Plasma-treated *Bombyx mori* cocoon separators for high-performance and sustainable lithium ion batteries

Rui F. P. Pereira,[1,] Renato Gonçalves,[1] Helena Rodrigues,[2] Daniela M. Correia,[2,3] Carlos M. Costa,[1,3,*] Maria M. Silva,[1] Senentxu Lanceros-Méndez,[4,5,*] Verónica de Zea Bermudez[2,*]*

[1]Chemistry Center and Chemistry Department, University of Minho, Campus de Gualtar, 4710-057 Braga, Portugal
[2]Chemistry Department and CQ-VR, University of Trás-os-Montes e Alto Douro, Apartado 1013, 5001-801 - Vila Real Codex, Portugal
[3]Physics Center, University of Minho, Campus de Gualtar, 4710-057 Braga, Portugal
[4]BCMaterials, Basque Center for Materials, Applications and Nanostructures, UPV/EHU Science Park, 48940 Leioa, Spain
[5]IKERBASQUE, Basque Foundation for Science, Bilbao, 48013 Spain

Corresponding Authors: *rpereira@quimica.uminho.pt; cmscosta@fsica.uminho.pt; senentxu.lanceros@bcmaterials.net; vbermude@utad.pt

KEYWORDS: *Bombyx mori* cocoon separators; plasma treatment; lithium-ion batteries; performance; safety; sustainability

Abstract

The success of lithium ion batteries (LIBs) and their unique advantages for electrochemical energy storage have speed up research in this field. A critical component of LIBs is the separator. Here, *Bombyx mori* silk cocoon separators have been treated with oxygen (O_2) and nitrogen (N_2) plasmas at different exposure times. The goal was to improve the electrochemical characteristics of these natural separators without jeopardizing the major attributes of silk fibers. Major physical and chemical modifications have been identified at the submicrometer scale upon the application of the plasmas: (1) Etching of the silk nanofibrils and concomitant increase of roughness (more effective with O_2 plasma), corresponding to the destruction of the 5^{th} structural hierarchy level of the silk fibers. (2) Creation of oxygen-containing functional groups carrying negatives charges at the surface, causing a superhydrophic-to-superhydrophilic transition, and favoring Li^+ transport. The optimized cocoon separator exposed to O_2 plasma for 30 s exhibited high electrolyte uptake (289%), high ionic conductivity (2.33 mS cm^{-1} at 25 ^oC) and low overall resistance. A cathodic half-cell of carbon-coated lithium iron phosphate incorporating this separator sample soaked in the ethylene carbonate/dimethyl

carbonate/lithium hexafluorophosphate electrolyte demonstrated a performance boost with respect to the battery including a raw cocoon separator: an outstanding increase (ca. 270%) of the discharge capacity (from 26.1 to 96.7 mAh g^{-1} at 5C-rate) and an impressive increase (291%) of the capacity retention (from 22.3 to 87.2%, from C/5 to 5C). This work proves that the O_2 plasma exposure is a valid, simple, fast, clean and safe top-down methodology to improve the properties of *Bombyx mori* cocoon separators. The features of these plasma-treated separators, which surpass those of commercial separators, help upgrading the performance of LIBs. This plasma-enhanced natural biomaterial separator technological platform pushes LIBs to the next performance-level, while guaranteeing the eco-friendly, sustainability and safety labels.

1. Introduction

Owing to their high energy density, high coulombic efficiency, low self-discharge features, quasi zero-memory, high open circuit voltage, and long lifespan, lithium-ion batteries (LIBs) represent promising energy storage devices which, as recognized by the 2019 Nobel Prize in Chemistry [1], stand at the forefront of the on-going technological revolution [2-7]. LIBs have made a tremendous impact on our society. Used in many popular devices, such as the ubiquitous smartphones, laptop computers, digital cameras, and tablets, they may be scaled to power cars, or miniaturized to power pacemakers.

The separator is a core component of LIBs [8-10]. It is placed between the cathode and the anode as a physical barrier, to ensure electronic insulation, and hinder short-circuit problems, while enabling ion transport. Although it is a non-electrochemically active component, the role of the separator is far from passive, influencing markedly the battery cost, life, reliability and safety. During LIB operation, high values of Li^+ ion conductivity and Li^+ ion transference number for the electrolyte in the separator pore spaces are essential to avoid deleterious degradation processes associated with heat generation and lithium plating. On the other hand, the ionic transport across the electrolyte-filled pore separator network must be homogeneous to mitigate the risks of incomplete lithiation/delithiation, and local overcharge. Lagadec et al. [9] highlighted that the separator structure (characterized by porosity, tortuosity, permeability, and connectivity), the separator chemistry (represented by the materials composition), as well as the separator/electrolyte interplay (measured by the electrolyte wettability), impact LIB performance.

Polyolefins have been the dominant separators of commercial LIBs in the past decades [11]. However, these polymers have major shortcomings which need to be tackled. They are hydrophobic materials offering poor compatibility with the liquid electrolyte. In addition, they undergo severe thermal shrinkage above 100 ºC because of their low melting points. Besides, they have low porosity, and exhibit poor mechanical properties. Currently, significant efforts are being made to obviate these disadvantages and to meet the greater demands that new applications place on LIB technology. The quest for durable, reliable, and safe separators, produced by means of cost-effective processes, and combining high ionic conductivity and excellent thermal stability, is imperative. One pathway to optimize the technology of separators is to gather inspiration from Nature. Natural polymers with multi-length-scale hierarchical structures are particularly attractive, because they are renewable, biocompatible, biodegradable, and low cost.

In the light of this bio-inspired approach, silk attracted our attention. Out of the class of natural fibers, silks, with a tradition of more than 5000 years in the textile industry, are deeply appreciated, mainly because of the lustrous appearance and soft touch of silk fabrics. Spun by certain arthropods (e.g., silkworms, spiders, scorpions, mites, bees and flies), silks are fibrous materials possessing a series of extraordinary attributes. Their unique mechanical behavior (high tensile strength and great extensibility), which outperforms that of the best available synthetic materials, is correlated with the presence of hierarchical mesoscopic structures [12]. As the fibers are non-toxic, biocompatible [13], and have controllable biodegradability, silk is regarded as an excellent biomaterial candidate for healthcare applications [14-17] and biological analysis [18]. Their heat-conducting ability, easy processing into films, and wide optical window have opened a wide range of potential new opportunities. Not surprisingly, a myriad of high-tech applications of silk-based materials in a variety of domains, spanning from lithography [19], optics [20, 21], photonics [22], and electronics [23-25], to energy [26-32], have emerged in the last decade. The vast majority of the research on silk-based materials and devices relied on the use of silk fibroin (SF) extracted from *Bombyx mori* silkworm cocoons. For instance, we proposed SF-based separators for LIBs [31]. In the native fiber, SF is a water-insoluble fibrous core protein with more than 5000 amino acids and high molecular weight (200 – 350 kDa or more), which is surrounded by silk sericin (SS), a water-soluble glue-like globular protein (10-300 kDa).

Owing to present safety and sustainability concerns, and to the pressing need to avoid the non-green and time/energy-consuming chemical procedures involved in the removal of SS from the

raw silk fibers (degumming process [33]), a part of the scientific community has turned its attention to the native silk cocoons. Although this challenging concept is still at infancy, several studies have successfully explored it and exciting future possibilities of application have been suggested [34-36]. We proposed that raw *Bombyx mori* silkworm cocoons are suitable bio-inspired environmentally friendly separators for the design of the next-generation of LIBs with improved sustainability and enhanced safety [32]. We showed that silkworm cocoons are a valuable alternative to polyolefins, offering several merits for LIBs [32]: (1) High degree of porosity (85 ± 27 %), ensuring electrolyte infiltration and Li^+ flow; (2) Thermal decomposition above ca. 280 ºC; (3) Good mechanical resistance; (4) Maximum electrolyte uptake values of the order of 300-400%; (5) Good electrolyte retention; (6) Preservation of the physical-chemical properties after battery operation; and (7) Self-extinguishing ability, contributing to reduce or eliminate fire risk. A LIB incorporating a cocoon separator soaked in the ethylene carbonate (EC)/dimethyl carbonate (DMC)/lithium hexafluorophosphate ($LiPF_6$) liquid electrolyte exhibited excellent cycling performance, with a discharge capacity of 86 mAh g^{-1}, and a capacity retention of 81% after 50 cycles at C-rate [32].

Motivated by the fact that plasma treatments applied over polyethylene membrane separators improved the performance of LIBs [37, 38], and also driven by the fact that the exposure of silk-based materials to several plasmas [39-45] exerted an important effect on the surface hydrophilicity, we decided to expose *Bombyx mori* silkworm cocoon separators to oxygen (O_2) and nitrogen (N_2) plasmas. The selection of these two reactive plasmas aimed at avoiding the introduction of different chemical species at the surface of the native protein fibers. Although both provide similar results, their use is in general dictated by the type of material to be treated or by the type of activation envisaged. Indeed, when they are applied, reactive functional groups including oxygen atoms (e.g., hydroxyl (–OH), carbonyl (C=O) and carboxylic (–COOH) groups) and nitrogen atoms (e.g., amine groups ($–NH_2$) groups), respectively, are formed at the surface of the material.

Herein, a comprehensive characterization of the surface of *Bombyx mori* silkworm cocoon separators exposed to O_2 and N_2 plasmas at various treatment times has been carried out using Atomic Force Microscopy (AFM) and X-ray photoelectron spectroscopy (XPS). The impact of both plasmas on the morphology, wettability, wicking and flammability of the materials has been evaluated. We demonstrate that the exposure of a raw cocoon separator to O_2 plasma for just a few seconds significantly boosted its electrochemical features (EC/DMC/$LiPF_6$ electrolyte uptake capacity, ionic conductivity and interfacial properties). The performance of

a cathodic half-cell with C-$LiFePO_4$ assembled with the cocoon separator sample featuring the best properties was investigated. The results obtained are very exciting, since they outrival those reported for analogue battery systems including some commercial separators.

2. Experimental

2.1 Materials

Bombyx mori cocoons were obtained from APPACDM (Castelo Branco, Portugal). Poly(vinylidene fluoride) (PVDF, Solef 5130, Solvay), lithium iron phosphate/carbon (C-$LiFePO_4$, Phostech Lithium), carbon black (Super P-C45, Timcal Graphite & Carbon), N-methyl-2-pyrrolidone (NMP, Fluka, 99.9 %), hexane (Sigma-Aldrich, 99.9 %) were used as received. Customized battery grade electrolyte 1 M solution of lithium hexafluorophosphate ($LiPF_6$) in ethylene carbonate (EC): dimethyl carbonate (DMC) (50:50 vol/vol) was purchased from Solvionic. The cocoon separators were dried at 60 ºC in vacuum overnight and stored in a dry argon-filled glove-box, prior to the analyses and battery assembly [46].

2.2 Preparation of surface plasma-treated Bombyx mori cocoon separators

Bombyx mori cocoon separators were prepared by directly cutting a 10 mm-diameter and 438 ± 80 µm-thickness disc from the cocoon (retrieved from the flattest part). The surface was then plasma treated in a Zepto plasma chamber Diener Electronics (Ø = 105 mm, L = 300 mm, V = 2.6 L) equipped with a 40 kHz radio frequency plasma generator at 100 W. Plasma treatments were performed during different period of times (15, 30, 50 and 100 s), at constant O_2 and N_2 flow, and under a total pressure of 80 Pa. *Bombyx mori* cocoon separators were prepared by directly cutting a 10 mm-diameter and 438 ± 80 µm-thickness disc from the cocoon (retrieved from the flattest part). The surface was then plasma treated in a Zepto plasma chamber Diener Electronics (Ø = 105 mm, L = 300 mm, V = 2.6 L) equipped with a 40 kHz radio frequency plasma generator at 100 W. A set of 40 cocoons were treated with plasma. Four groups of 5 cocoons were exposed to a constant flow of O_2, during 15, 30, 50 and 100 s, under a total pressure of 80 Pa. The procedure was repeated with another set of 4 × 5 cocoons with N_2 plasma using the same experimental conditions.

2.2 Characterization of the separators

High Resolution Scanning Electronic Microscopy (HR-SEM) micrographs were obtained using a FEI Quanta 400 FEG microscope. Elemental analysis was performed by Energy Dispersive Spectroscopy (EDS) using an EDAX PEGASUS X4M. Prior to being analyzed, the samples were coated with gold/palladium.

Attenuated Total Reflectance (ATR)/ Fourier Transform Infrared (FT-IR) spectra of the separators were obtained in an IRAffinity 1s Fourier Transform Infrared Spectrophotometer – Shimadzu, equipped with a diamond crystal. Prior to measurement, a small piece of each sample was transferred to the diamond crystal and pressed. The spectra were recorded at room temperature in the 4000-400 cm^{-1} range by averaging 200 scans and a resolution of 4 cm^{-1} using the LabSolutions IR software.

AFM analysis was performed in an AFM CSI Nano-Observer equipment (Scientec) in tapping mode using a super sharp Si HQ:NSC19/FORTA probe with a frequency resonance of 60 kHz and a spring constant of 0.3 N m^{-1}. In order to improve the images quality a flattening and elimination of line noise tools were applied using the Gwyddion 2.54 software. To use this technique with a sample with high topographical map like a cocoon, it was necessary to restrict the analysis to individual fibers carefully removed from the cocoon surface. The individual fibers were immobilized in the AFM sampler disk, using double tape glue on each extremity. The fibers were handled in such a way that the surface to be analyzed was never in contact with the tweezers used during the immobilization procedure. Each fiber was mounted in order to assure that it was stretched and clipped only on the extremities. To guarantee that the images acquired were representative 2-3 cocoons subject to the same plasma time exposure were examined. From each cocoon 5 individual fibers were removed. Each fiber was analyzed on 3 different locations. Each of these samples was evaluated using a cantilever/fiber approach angle of 0 and 90º.

The XPS measurements were acquired in a Kratos AXIS Ultra HSA spectrometer using a monochromatic Al K_{α} radiation (1486.7 eV). XPS spectra were analyzed using the XPSPEAK 4.1 software and deconvoluted using the non-linear least squares fitting routine. The background was revised using the Shirley-type correction and The C_{1s} band at 284.6 eV was used as internal standard to rectify probable deviations caused by electric charge. Elementary atomic percentages were determined through peak areas analysis using the sensitivity factors indicated by the manufacturer.

The wettability of the cocoon samples was evaluated by means of water static contact angle measurements using the sessile drop method. Experiments were performed in a temperature-controlled chamber at 26 ± 1 ºC using a Krüss DSA25S drop shape analyzer controlled by the software ADVANCE. The volume of the liquid droplets (5 µL) was kept constant. Contact angles were determined from digital images acquired by a video camera using the Young-Laplace fitting. The contact angle values were measured from at least two different discs at 5 different spots. At each spot 5 measurements were performed. Contact angles values correspond to the average of all the measurements and the error corresponds to the arithmetic mean of the root mean square error. Additionally, one drop (2.5 µL) of methylene blue dye aqueous solution (1 g L^{-1}) was released on the cocoon separators. After the solution dried, the dispersion of the dye on the separators surface was estimated.

The flammability of the cocoon separators was evaluated using the plastic identification burn test [32].

The uptake values were obtained by immersing the cocoon separators into the EC/DMC $LiPF_6$ electrolyte and using the relation:

$$uptake = (m_i - m_0)/m_0 \times 100 \quad (1)$$

where m_0 is the mass of the dry cocoon, and m_i is the mass of the cocoon after immersion in the electrolyte.

The ionic conductivity (σ_i) of the cocoon soaked in the EC/DMC $LiPF_6$ electrolyte was calculated by complex impedance spectroscopy in the 65 kHz-500 mHz frequency range, with an amplitude of 10 mV, at 25 ºC, using an Autolab PGSTAT-12 (Eco Chemie) equipment. The sample was placed in a constant volume support equipped with gold blocking electrodes located within a Büchi TO 50 oven. The σ_i value was determined using the equation:

$$\sigma_i = d/(R_b \times A) \quad (2)$$

where d is the thickness, R_b is the bulk resistance, and A is the area.

2.3 Battery preparation and characterization

The battery cathode was prepared by mixing C-$LiFePO_4$ (active material), Super P-C45 (conductive additive), and PVDF (polymer binder) in NMP with a weight ratio of 80:10:10 (wt.%), corresponding to 1 g of solid material for 2.25 mL of NMP. The electrodes were dried at 90 ºC in vacuum overnight before being transferred to the glove-box [46]. The active mass

loading, thickness and porosity of the electrodes were ~1 mg cm^{-2}, 20 µm and 75 %, respectively. Two electrodes Swagelok type cells for Li/C-$LiFePO_4$ half-cells were then assembled in a homemade argon-filled glove box. The prepared half-cells have a metallic lithium foil (8 mm diameter) used as counter/reference electrodes, a 10 mm-diameter *Bombyx mori* cocoon soaked into electrolyte EC/DMC/$LiPF_6$ used as separator and the previously prepared C-$LiFePO_4$ electrode film (8 mm diameter) used as cathode. The cycling performance of the Li/C-$LiFePO_4$ half-cells was evaluated through galvanostatic measurements at room temperature using a Landt CT2001A Instrument from 2.5 to 4.2 V at scan rates, C/5 to 5C (C =170 mA g^{-1}). The electrical properties of the Li/C-$LiFePO_4$ half-cells were measured before and after cycling by complex electrochemical impedance spectroscopy (EIS) using an Autolab PGSTAT12 instrument in the 1 MHz - 10 mHz frequency range with an amplitude of 10 mV.

3. Results and discussion

3.1 Impact of the plasma treatment on the physical-chemical properties of the Bombyx mori cocoon separators

The surface modification of polymer fibers (natural or synthetic) is of large relevance in the areas of textiles [47] and biomedical engineering [48], among others. Over the last few years, plasma treatments have gathered increasing attention, as they offer major advantages with respect to conventional wet processes in terms of environmental footprint and health concerns. Plasma treatments are fast, affordable, safe, reliable and dry processes, which do not produce waste or contaminations, and involve very low chemical consumption. In addition, they have low range of penetration (a few nm skin depth), modifying solely the uppermost atomic surface layers of the substrate, but leaving the bulk properties unaffected [49].

Plasma can be described as a complex mixture of electrons, neutral atoms and molecules [50]. There are three major classes of plasmas according to the way the gas employed is consumed [51]: (1) chemically non-reactive plasmas (inert monoatomic gases, such as argon (Ar)); (2) chemically reactive plasmas (inorganic or organic molecular gases, such as O_2, N_2, hydrogen (H_2), sulfur hexafluoride (SF_6), and methane (CH_4)) which, despite their reactivity, do not form polymeric deposits on the pure gas plasma; (3) polymer forming plasmas, i.e., reactive plasmas which form a polymeric solid deposit by themselves. Apart from exerting changes in the surface chemistry, plasma treatments may also affect the surface topography. Depending on the plasma gases and on the parameters applied, it is possible to clean, activate, etch, and/or coat a specific

surface. Typical applications of plasma treatment range from the cleaning of the surfaces of medical equipment to the activation of the surface of textile fibers [52, 53]. As a result of the chemical and/or physical changes produced, the hydrophilicity/hydrophobicity, wicking, wetting, shrink resistance, tensile strength, flame retardance, biocompatibility, and anti-bacterial properties of the fibers may be significantly improved.

To understand the physical perturbation caused by the O_2 and N_2 plasmas on the cocoon fibers and to get insight into the influence of the plasma treatment time on the topography of the silk fibers of the *Bombyx mori* cocoons, an AFM analysis was performed. In the measurements *quasi* perpendicular (~0 º) and *quasi* parallel (~90 º) configurations of the cantilever with respect to the fiber axis were considered (Figures 1 and 2, respectively).

Before starting the discussion of the AFM data, it is fundamental to mention how silk materials are organized. The five levels of hierarchical structure of silks were recently reviewed [54]. Level 1 comprises the amino acid sequence within the protein molecules. Level 2 is associated with the regular hydrogen bonding pattern between the amine and carboxyl groups which gives rises to the formation of α-helices and β-sheets (and β-turns). Level 3 refers to the three dimensional (3D) and highly compact structure essentially composed of intermolecular β-crystallites. Level 4 regards the molecular β-crystal network (nanofibrils) [55], in which amorphous chains bond the β-crystallites together along a nano-fishnet topology. The interconnectivity between nanofibrils gives rise to the formation of a network of nanofibers (multi-domain system) which is addressed as Level 5. For instance, it was reported that SF fibers exhibit a system of strong domain–domain interactions, because the fibers are composed of a bundle of highly well-oriented, twisted nanofibrils that are interlocked by adjacent nanofibrils, to guarantee that the nanofibrils cannot move freely [56]. It must be emphasized, however, that the physical dimensions, morphology, and spatial organization of the nanofibrils in silk fibers have sparked an intense debate that led to the development of many structural models [57].

Figure 1 shows the damage produced by the O_2 and N_2 plasmas on the surface of an individual fiber for different treatment times. The exposure to O_2 plasma for 15 s led to the cleavage of nanofibrils (Figure 1Ab). With increasing exposure time ($t \geq 30$ s) deep cavities were carved in the inner structure of the fiber. Figures 1Ac-e reveal aligned nanofibrils with a unique "spaghetti-like" pattern. From the AFM data of the cocoons treated with O_2 plasma, the average roughness values of the fibers were calculated (Figure 1C, red symbols). Upon exposure with O_2 plasma treatment for 15 s, the average roughness value of the raw fibers increased from 9.9

to 16.0 nm, presumably because the initial etching of the fibers led to a marked mismatch of the nanofibrils (Figures 1Ab and 1Ac). Figure 1Ac shows that upon further increasing the O_2 plasma exposure time to 30 s, the formation of cavities between the nanofibrils became more important, while leaving the nanofibrils perfectly aligned. These observations strongly suggest that the energy employed at this point was almost exclusively used to break the nanofibrils and form cavities. As a consequence, the average roughness was minimum at this stage (9.1 nm). At higher O_2 plasma exposition time (t = 50 s) (Figure 1Ad), the medium roughness of the fibers increased to 12.4 nm, as the diameter of the cavities and the mismatch between the nanofibrils increased. The situation was identical in the case of sample treated with O_2 plasma for 100 s (Figure 1Ae), for which the average roughness remained constant (12.6 nm). However, both effects compensated each other, and as a result the roughness values for the latter two samples remained lower than that of the sample treated with O_2 plasma for 15 s.

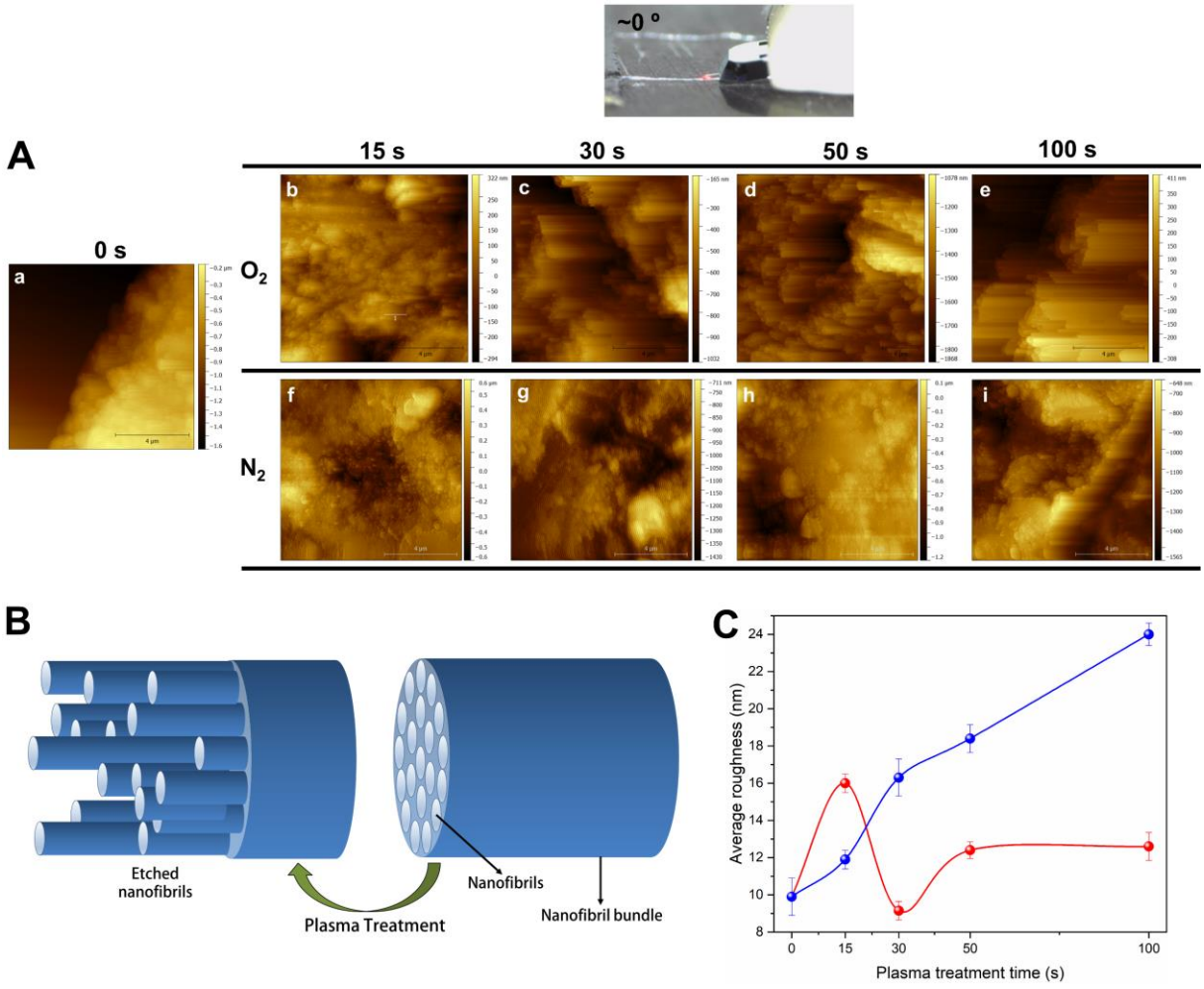

Figure 1. (A) AFM images of an individual silk cocoon fiber acquired with a 0 º configuration between the cantilever and the fiber axis and in tapping mode at 10 µm of the sample, before

(a) and after exposure to O_2 (b-e) and N_2 (f-i) plasmas. (B) Schematic representation of the etching effect caused by the O_2 and N_2 plasma treatments on the nanofibrils. (C) Exposure time dependence of the average roughness deduced from the AFM data for the *Bombyx mori* silk cocoon separators treated with O_2 (red symbols) and N_2 (blue symbols) plasmas. The lines are just guides for the eyes.

The AFM data provided evidences of significant differences between the O_2 and N_2 plasma treatments. Indeed, although the same structural effects (i.e., etching and cavity formation) were distinguished, in the N_2-treated samples, they both evolved at a considerably slower rate. With the latter treatment the cavities were only formed at an exposure time of 100 s (Figure 1Ai) versus only 30 s for O_2 plasma (Figure 1Ac). This interesting finding can be explained in terms of the higher reactivity of O_2, which is known to exert a more effective and faster etching. Not surprisingly, the surface roughness of the N_2 plasma-treated samples increased regularly with the treatment time (Figure 1C, blue symbols), indicating that the etching caused by this gas took place progressively at a slower pace than O_2. It is noteworthy that after an exposure time of 100 s to N_2 plasma the average roughness of the separator was 24.0 nm, thus twice higher than that of the corresponding O_2 plasma-treated sample (12.6 nm). The lower molecular weight of the N_2 gas, probably diffusing more easily inside the silk fiber, and thus affecting it in a much more uniform way, might explain these results.

The acquisition of the AFM images with the cantilever aligned at 0 º with the fiber, and the use of a sharp tip, enabled us, not only to travel to the core of each individual fiber, and perceive the nanofibrils, but also to observe the etching produced by the plasma treatment that led to a mismatch between the nanofibrils where the chemical bonds were disrupted. This effect is quite interesting. The generation of silk nanofibrils via top-down physical or chemical disintegration was reported by several authors. Zhao and Feng [58] described the production of *Bombyx mori* nanofibrils by the ultrasonic technique through the application of 900 W for 30 min using water as sole solvent. Ling et al. [25] directly exfoliated silk fibers on the single nanofibril level, by integration of chemical (partial dissolution) and physical (ultrasonic dispersion) methods, by means of a three-step route involving hexafluoroisopropanol (HFIP) as solvent. More recently, Tang et al. [59] reported a facile, high-efficiency, and scalable liquid exfoliation method to directly extract silk nanofibrils from silk fibers using protein denaturant deep eutectic solvent urea/guanidine hydrochloride. To the best of our knowledge, the plasma-induced etching of the cocoon nanofibrils, performed in a matter of seconds and demanding no solvents, was never

reported previously by AFM, in spite of the fact that a few studies on silks employed this technique [60-63].

We must note that the 2- and 3D AFM images shown in Figure 2 indicate that the etching effect was, in contrast, completely blurred when the same tip was used with a 90 º cantilever/fiber configuration (Figure 2).

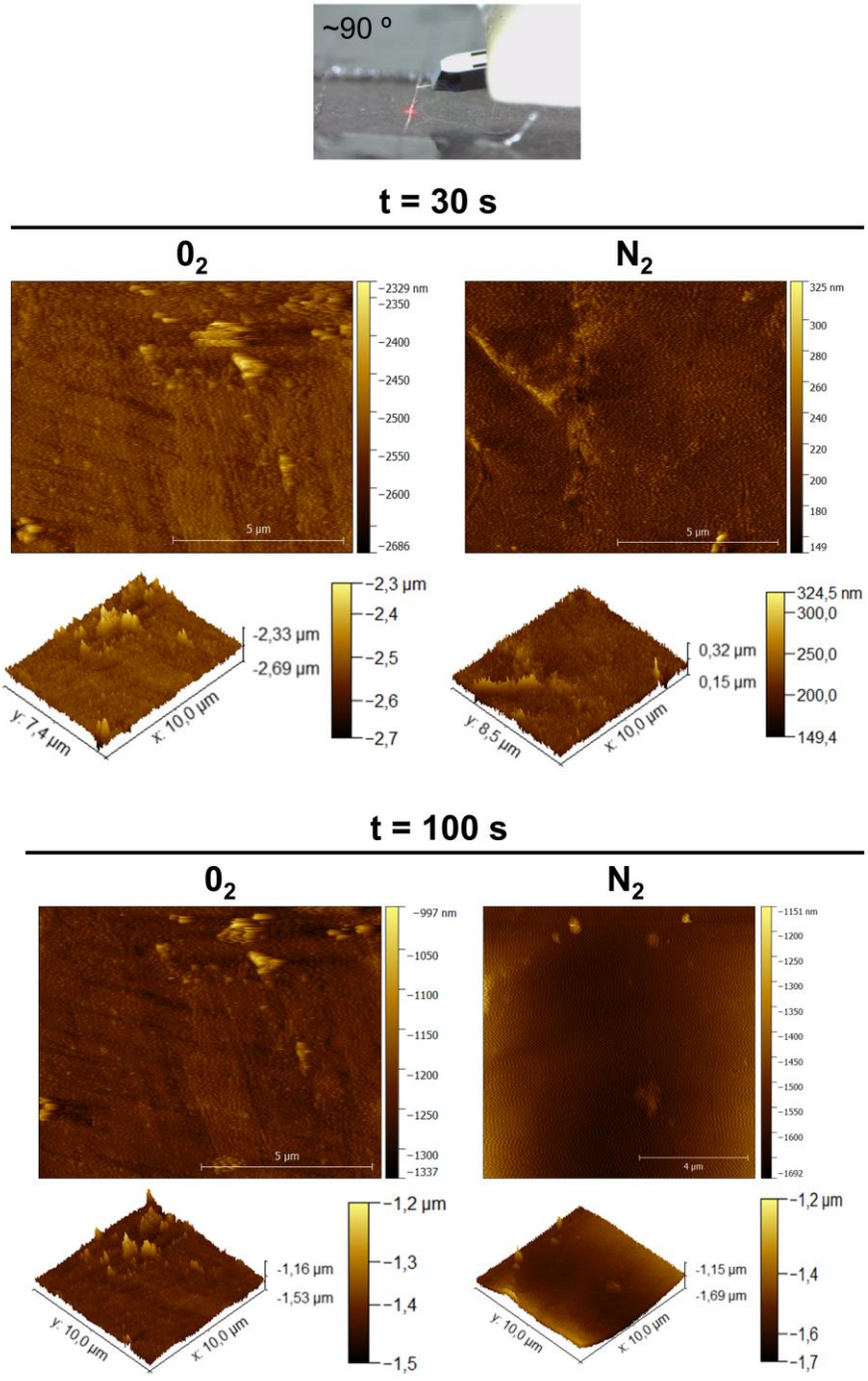

Figure 2. 2D (top) and 3D (bottom) AFM images of an individual cocoon fiber, acquired in a 90 º configuration between the cantilever and the fiber, in tapping mode at 10 μm of the samples, after exposure to O_2 and N_2 plasmas for 30 and 100 s.

Because the topographical changes observed in the surface of the *Bombyx mori* cocoon fibers after exposure to O_2 and N_2 plasmas occurred much sooner in the case of the former plasma, the discussion of the XPS and ATR/FTIR data that follows, devoted to the assessment of the chemical changes produced in parallel by the plasma treatment, will be essentially focused on the separator sample treated with O_2 plasma. The XPS data obtained for the cocoon sample treated with N_2 plasma can be found in Appendix A (Table A.1).

The XPS data obtained for the cocoons in the raw state and treated with O_2 plasma under different exposure times are represented in Figures 3 and summarized in Appendix A (Table A.1). We must stress that, given the inherent heterogeneities of this natural fiber, this study was extremely difficult and, as such, the results were interpreted with extreme care. To minimize misleading conclusions, at least three different analysis spots of each cocoon were considered and an average value was obtained.

Figure 3 quantifies the presence of carbon (C), nitrogen (N) and oxygen (O) at the surface of the separator. The error bar included in Figure 3 reflects the dispersion of results from the XPS analysis. The atomic surface composition was evaluated from C1s, N1s and O1s scanning spectra. Examples of XPS spectra are presented in Appendix A (Figure A.1a). The C1s spectra (Figure A1b) present three peaks centered at around 285, 286 and 288 corresponding to C-C and C-H, C-OH, and C=O ether and N-C=O amide bonds, respectively [64, 65]. Single peaks are observed at 399 eV (Figure A1c) and 531 eV (Figure A1d), which can be ascribed to the N and O atoms, respectively [64, 65].

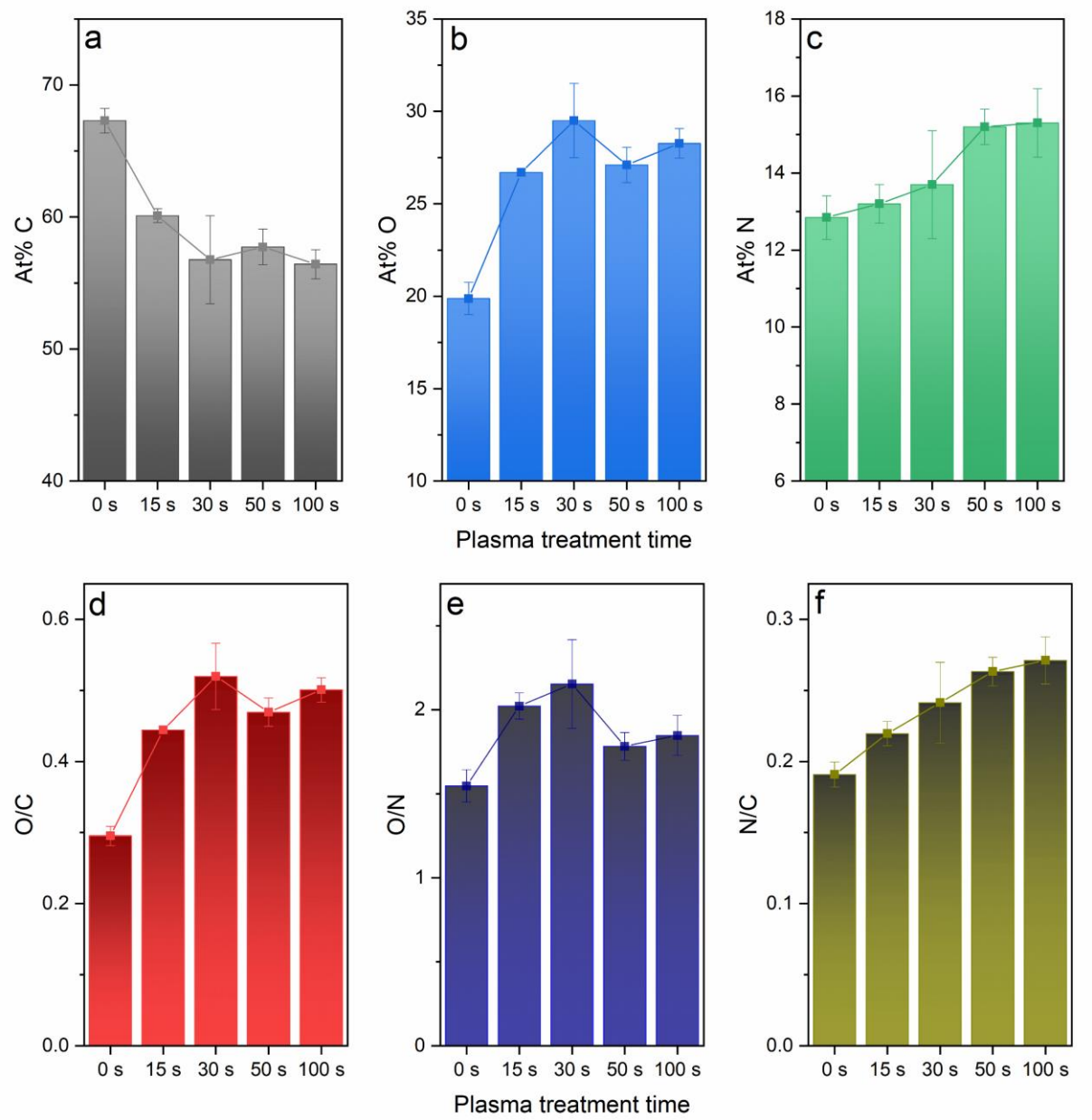

Figure 3. Elemental composition (C – grey bars, O – blue bars, N – green bars) (a-c) and elemental ratios (C/O – red bars, O/N – navy bars, and C/N – dark yellow bars) (d-f) at the surface of *Bombyx mori* cocoon separators as a function of O_2 plasma exposure time.

After being exposed to O_2 plasma for 15 and 30 s, the treated cocoons exhibited lower C content (Figure 3a), but increasingly higher O and N contents (Figures 3b and 3c, respectively) with respect to the raw cocoons. The highest amount of O in the cocoon surface was reached after 30 s plasma treatment. For treatments involving higher exposure times (t = 50 and 100 s), the C, O and N contents were not practically altered. These global changes are also visible in the trends of the O/C and N/C ratios (Figures 3d and 3f, respectively), with highlight to the

maximum ratio O/C being reached for 30 s. Clearly, the treatments lasting 15 and 30 s were the most critical, leading to severe scission of the peptide chains and to the cleavage of the side chains of the amino acids. As a consequence, the C content of the fibers was markedly reduced, yielding volatile compounds (e.g., CO, CO_2). As usual in this sort of processes, free radicals were also produced at the surface of the fibers, which readily reacted with atmospheric air (O_2, N_2, water vapor), explaining why the O and N content increased in the fibers. It is also interesting to notice from the XPS data that the average binding energy did not change significantly with plasma exposure, suggesting that new chemical bonds, functional groups or radicals were apparently not formed.

As pointed out by AFM, the N_2 plasma treatment was a slower process that eventually led to the same topographical result. The XPS data of the N_2 plasma-treated samples substantiate this explanation. Indeed, Figure A.2 (Appendix A) shows that there is not a marked trend of the N atomic percentage with plasma exposure time. The maximum content of O and the highest O/C ratio were only reached after 100 s, even though there is a local maximum of these values for 30 s.

To further examine the chemical modifications produced by the O_2 plasma on the cocoon fibers, we inspected the ATR/FT-IR spectra (Appendix A, Figure A.3). Our attention was focused in particular on the amide I and amide II spectral regions, reproduced in Figure 4, because both provide useful information on the extent and strength of hydrogen bonding interactions.

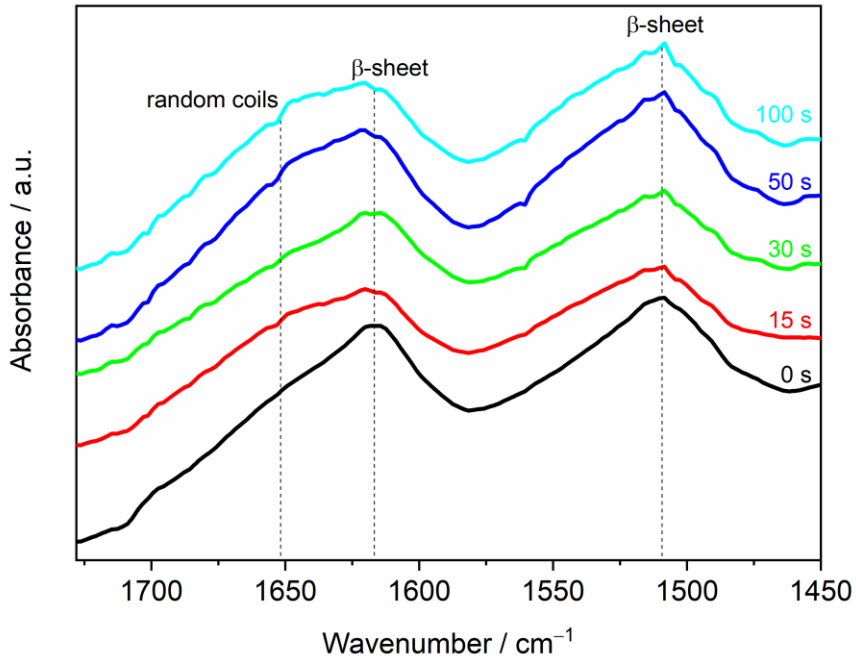

Figure 4. ATR/FT-IR spectra of the *Bombyx mori* cocoon separators in the amide I and II regions: raw (black line) and O_2 plasma-treated with different exposure times.

The spectra are very similar. Prominent amide I and amide II bands with intensity maxima at 1616 and 1508 cm^{-1}, respectively, are evident in all cases. Interestingly, upon O_2 plasma treatment, no significant shift of these bands occurred, indicating that the magnitude of the hydrogen bonding interactions was globally not affected. The emergence of a shoulder around 1650 cm^{-1} in the amide I band profile of all the treated samples except in that exposed to O_2 plasma for 30 s is, however, clearly evident. The growth of the 1650 cm^{-1} component in the samples exposed to O_2 plasma for 15, 50 and 100 s may be correlated with an increase of the relative proportion between the random coils and β-sheet conformations [51-53]. Thus, we may speculate from these data that in the case of the cocoon separator sample treated for 30 s no breakdown of β-sheets occurred. In practice this seems to indicate that the mechanical properties of this treated sample remained unaltered with respect to those of the native cocoon. These findings may be correlated with the fact that in this sample, according to AFM, while the formation of cavities between the nanofibrils was noteworthy, the nanofibrils remained unaltered and perfectly aligned.

The AFM, XPS and ATR/FT-IR analyses provided evidences that the O_2 plasma treatment exerted a much more marked etching effect on the surface of the *Bombyx mori* cocoon separators than the N_2 plasma. A key conclusion retrieved from these data is that the nature of the changes arising from the exposure to both plasmas is apparently more physical/topographic than chemical.

3.2 Characterization of the plasma treated Bombyx mori cocoon separators

3.2.1 Morphology, wettability, wicking and flammability

The SEM images of the outer and cross sections of *Bombyx mori* cocoon separators in the raw state (0 s) and treated with O_2 plasma during different periods of times (between 15 and 100 s) reveal that the non-treated and treated fibers exhibit a smooth and relatively clean surface, showing no evidences of the removal of the SS layer (Figure 5). The characteristic random distribution, interconnectivity, high porosity, multilayer structure, and diameter of the fibers were preserved after application of the plasma treatment. These evidences confirm that the O_2

plasma did not alter the morphology of the native cocoons at the microscale. In the case of the N_2 plasma, the same conclusion was reached (data not shown).

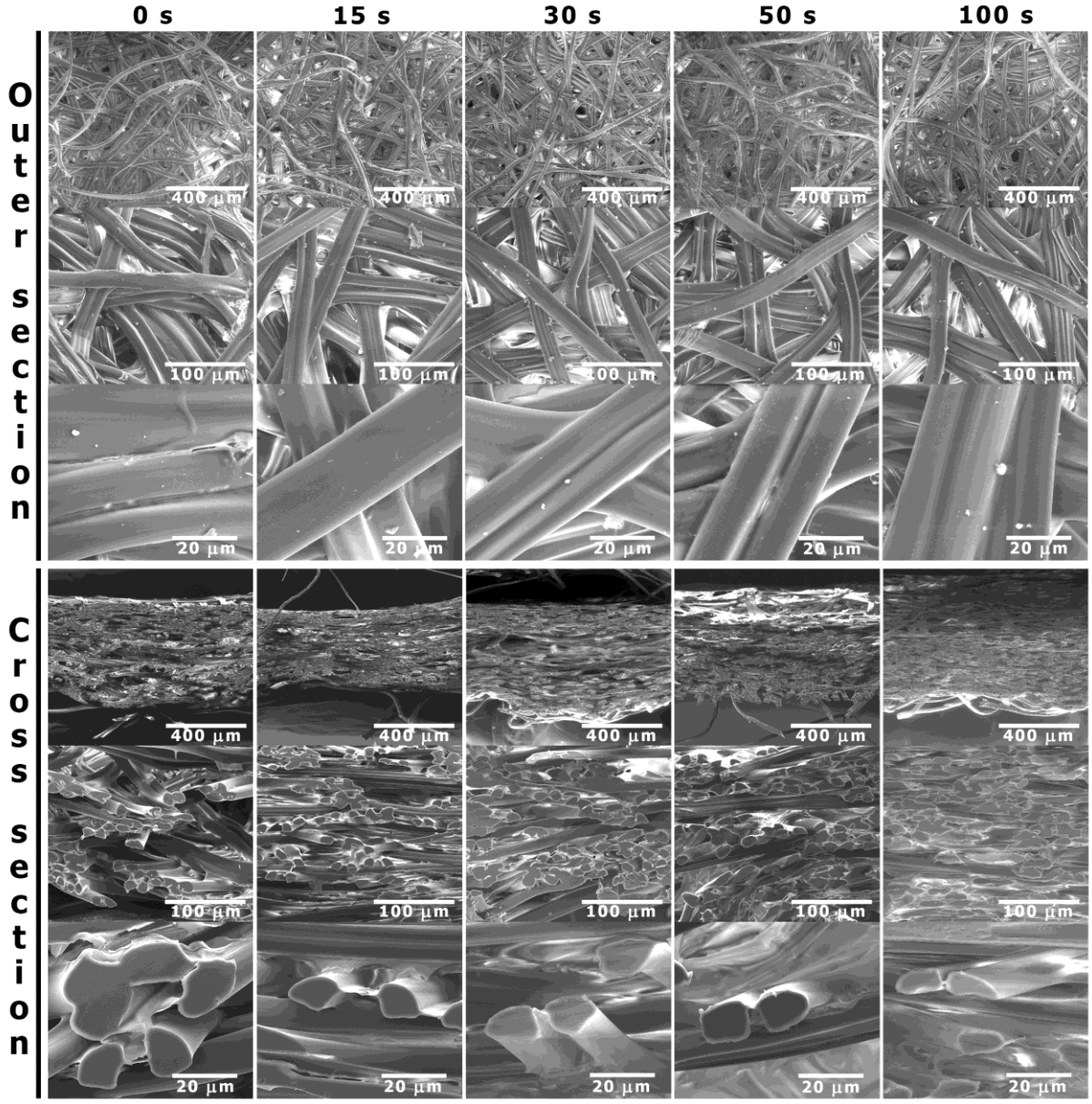

Figure 5. SEM images of the outer section and cross-section of *Bombyx mori* cocoon separators: raw (0 s) and treated with O_2 plasma.

The O_2 plasma treatment is known to exert a strong impact on the wettability of materials [44, 45, 66, 67]. Accordingly, the superhydrophobic behavior of the outer surface of the raw *Bombyx mori* cocoons (average water contact angle of 147±9 º) (Appendix A, Figure A.4) was strongly affected by O_2 plasma treatment, independently of the exposure time. No contact angle

measurements could be performed in the treated cocoons, because the drops of water were immediately adsorbed by the cocoon surface. It seems thus reasonable to assume that the contact angle became virtually 0 º in the O_2 plasma-treated cocoon fibers even for the lowest irradiation time considered (15 s). These findings reveal that the cocoon surface changed from superhydrophobic to superhydrophilic. The N_2 plasma treatment led exactly to the same results. The impressive reduction of the water contact angle value observed is a clear indication that the wettability of the cocoon fibers was dramatically increased.

When water is placed in contact with a porous material and the surface is superhydrophilic, wicking occurs. This phenomenon, governed by capillary action, drives water in capillary spaces. As a consequence, water attempts to spread across the surface. A simple test using a methylene blue dye aqueous solution was performed in order to estimate *grosso modo* planar wicking on the surface of the cocoon separators. One drop of the dye aqueous solution was placed on the top of the cocoon separators and after 2 min the surface was inspected. Figure 6a shows that in the case of the non-treated superhydrophobic cocoon sample, no spreading occurred. Instead the formation of a spherical drop was visible. In the case of the superhydrophilic samples treated with O_2 plasma, the drop of the dye aqueous solution was spread out. In the case of the sample treated for 15 s, the area where the drop fell exhibited a circle with a dark blue color surrounded by an aureole with light blue color. The darker central area became progressively less pronounced at increasing plasma treatment time, pointing out increasing wicking. When water was replaced by the electrolyte mixture EC/DMC/$LiPF_6$, the drop of liquid was immediately adsorbed by all samples (raw and treated with O_2 and N_2 plasmas), thus preventing any contact angle measurements. Although it was not possible to quantify the phenomenon, the EC/DMC/$LiPF_6$ adsorption was, however, clearly higher for the treated samples (see supplementary information video).

The drastic alteration of the hydrophobicity/wettability/wicking of the cocoon separators upon treatment with O_2 and N_2 plasmas is in perfect agreement with the tremendous impact exerted by both these gases on the surface of the cocoon separators, as described in detail above.

A flammability test was performed to check whether the plasma treatments affected the inherent characteristics of the raw cocoon separators. Figure 6b reveals that the behavior of the sample which had been exposed to O_2 plasma for the longest time condition (100 s) matched that of the raw cocoon: it first ignited, and before the flame self-extinguished a small portion of it burned.

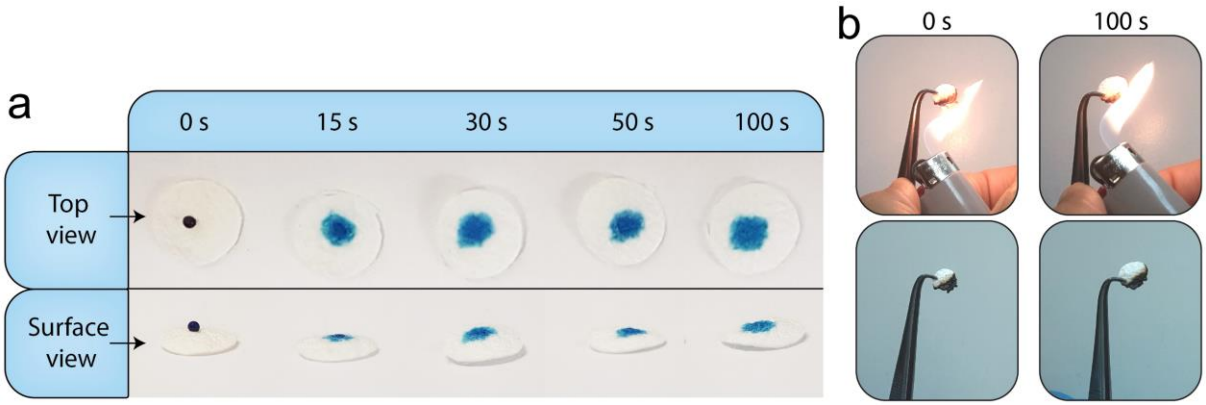

Figure 6. (a) Wicking and (b) flammability (initial (top) and final (bottom) steps) of raw and O_2 plasma-treated *Bombyx mori* silk cocoon separators.

3.2.2 Electrolyte uptake capacity, ionic conductivity and interfacial properties

Considering that the exposure of the surface of the *Bombyx mori* cocoon separators to O_2 plasma was very efficient, since it happened much sooner than in the case of N_2 plasma treatment, we decided to pursue the work by evaluating the electrochemical properties of the separators exclusively treated with O_2 plasma.

The electrolyte uptake capacity (in %) is a fundamental parameter that allows evaluating the electrolyte/separator interaction. The higher the uptake value, the higher the capacity of the electrolyte to remain inside the separator, and the stronger the interaction, enabling good Li^+ ion mobility across the separator during battery operation. The EC/DMC/$LiPF_6$ electrolyte uptake capacity values of the cocoon separators as a function of the dipping time were deduced from equation (1) and are represented in Figure 7a. The high uptake values observed may be correlated with the high porosity of the samples [32], evidenced by SEM (Figure 5). The maximum uptake percentage value was reached after ca. 15 s of dipping the cocoon separator in the electrolyte, with the exception of the non-treated cocoon separator that needed 2 min to reach the maximum uptake percentage. Further, the plasma treatment led to a decrease of the maximum uptake percentage value of the samples from 400% in the case of the raw cocoon to around 250-350% for the treated cocoon separators, the uptake value being scarcely affected by the plasma treatment time.

Figure 7b reproduces the Nyquist plots of the electrolyte/cocoon separators at 25 ºC. Figure 7c allow inferring, not only that the O_2 plasma treatment increased, as sought, the ionic conductivity of the cocoon separators with respect to that of the raw cocoon, but also that the

O_2 plasma exposure time altered the ionic conductivity in a non-linear fashion. At 25 ºC, while the non-treated cocoon separator exhibited an ionic conductivity of 0.43 mS cm^{-1}, the values found for the O_2 plasma-treated cocoon separators were 1.78, 2.33, 1.57 and 1.12 mS cm^{-1} for time exposures of 15, 30, 50 and 100 s, respectively (Figure 7c). In theory all these samples lend themselves for application as separators in LIBs, since the minimum conductivity required is 0.1 mS cm^{-1}. The maximum ionic conductivity was achieved for an O_2 plasma treatment of 30 s. This result beautifully correlates with the XPS data which revealed maximum contents of O, and of O/C and O/N ratios in the same sample.

To assess the interfacial properties between the cocoon separator and the cathode, half-cells versus Li^+ were prepared and impedance spectroscopy measurements were carried out prior to cycling measurements (Figure 7d). The typical Nyquist plot behavior of this assembly was composed of a linear region and a semicircle at low and high-medium frequencies, respectively. The linear region corresponds to Li^+ ion diffusion in the cathode active material. The semicircle is associated with the overall resistances (contact film, ohmic and charge-transfer reactions resistances), which are estimated through the equivalent circuit illustrated in the insert of Figure 7d). This equivalent circuit is typically used to analyze the electrical properties of battery separators Zhang, Z.; Wang, G.; Lai, Y.; Li, J.; Zhang, Z.; Chen, W. Nitrogen-Doped Porous Hollow Carbon Sphere-Decorated Separators for Advanced Lithium-Sulfur Batteries. J. Power Sources 2015, 300, 157−163. The straight line in the low frequencies range is described by a Warburg impedance related to the mass transport component. The overall resistances obtained for the cocoon separators were 562, 322, 323, 754 and 808 Ω for exposure times to O_2 plasma of 0, 15, 30, 50 and 100 s, respectively. The formation of the solid electrolyte interface (SEI) layer between the electrode and the electrolyte interface was evident. The SEI layer exhibited lower resistance in the cocoon separators treated for 15 and 30 s.

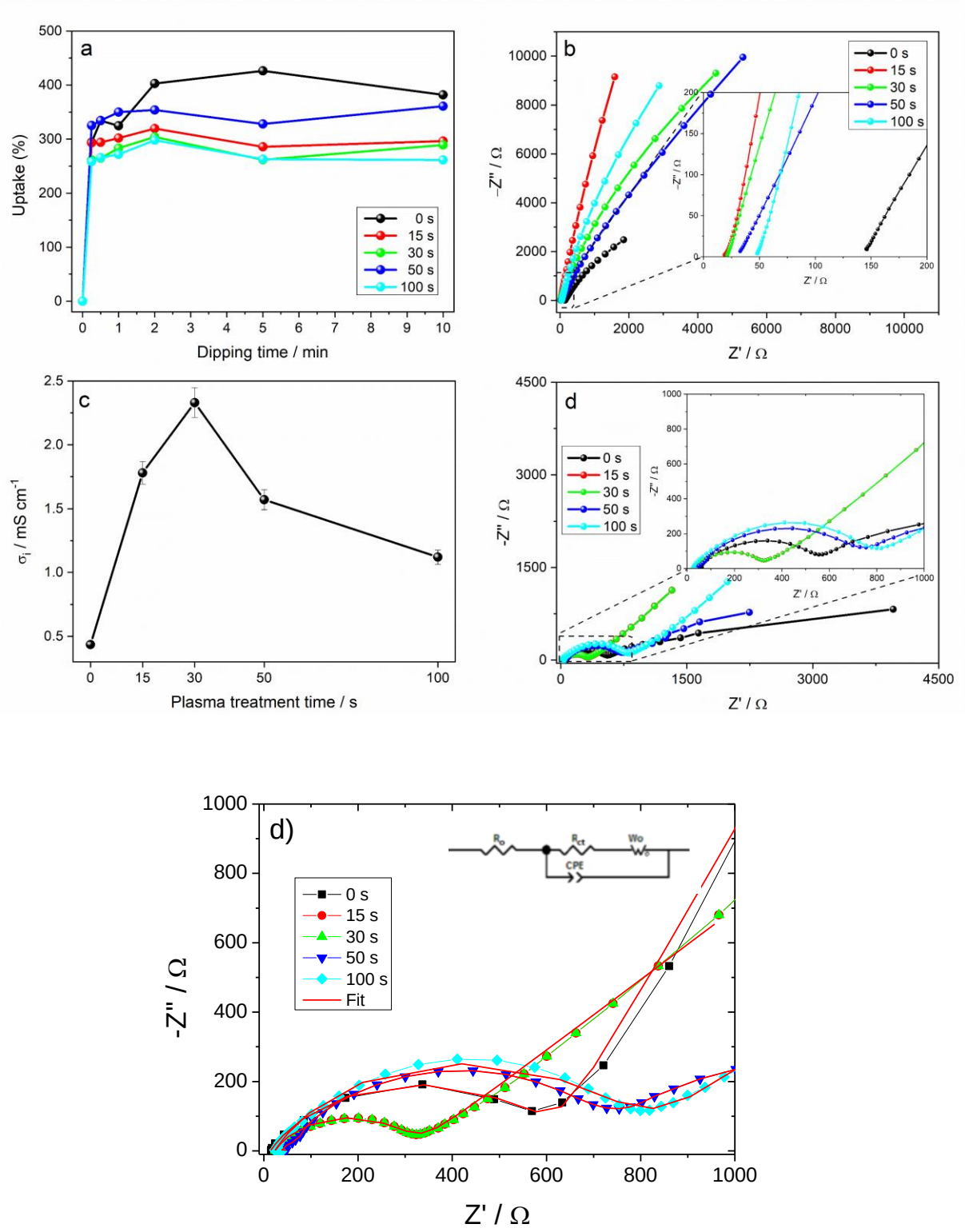

Figure 7. *Bombyx mori* cocoon separators treated with O_2 plasma. (a) Electrolyte uptake value of as a function of dipping time. (b) Nyquist plots and (c) ionic conductivity at 25 ºC of the separator soaked in the EC/DMC/$LiPF_6$ electrolyte. (d) EIS of the half-cell batteries before cycling as a function of plasma exposure time with the corresponding fit with the equivalent circuit presented in the inset. The lines drawn are guides for the eyes.

3.3 LIB performance

The electrochemical performance of the cocoon separators at different O_2 plasma treatment times was evaluated in half-cells of LIBs with charge and discharge cycles at different C-rates and cycle numbers. The C-rate study (C/5, C/2, C, 2C and 5C), and the cycle number study (55 cycles) at same C-rate were performed at room temperature between the 2.5 and 4.2 V. The results obtained are reproduced in Figure 8.

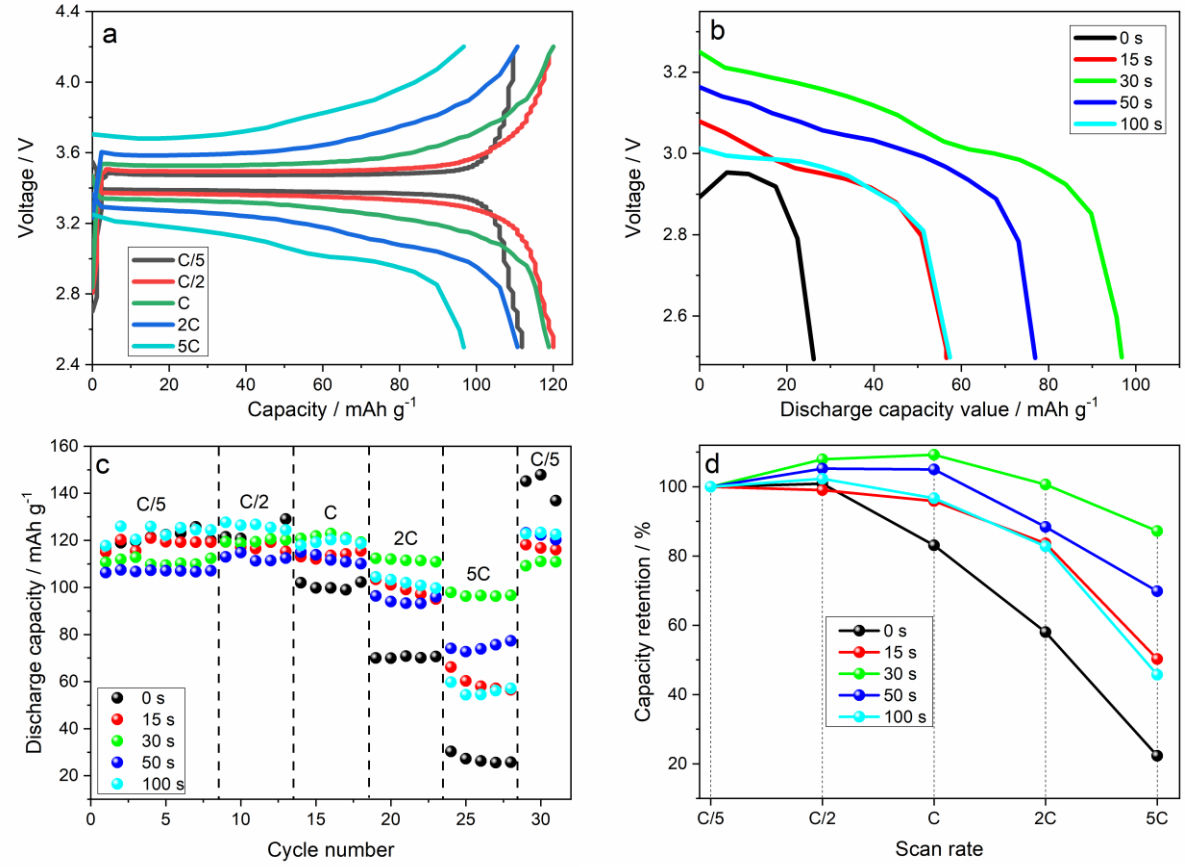

Figure 8. Performance of half-cell batteries including the cocoon separators treated with O_2 plasma. (a) Charge and discharge C-rate profiles (plasma exposure time of 30 s). (b) 5th discharge curves at 5C-rate. (c) Rate performance as a function of the cycle number and plasma exposure time. (d) Capacity retention as a function of plasma exposure time.

All the O_2 plasma-treated samples produced the same profile curves for the charge and discharge processes (Figure 8a), characterized by a flat plateau at about 3.2 V (discharge) and 3.7 V (charge) [68]. The 5th charge and discharge profile curves of the sample plasma-treated for 30 s at different C-rates are shown in Figure 8b. The two characteristic voltages observed, one for the charge and the other for the discharge, characterize the disinsertion and insertion of

the Li^+ ion in the C-$LiFePO_4$ structure, respectively. These phenomena occur due to the iron redox reactions (Fe^{3+}/Fe^{2+}) in the spinel $LiFePO_4$ structure [68]. With the increase of the C-rate, the cycling profile decreased (C/5 is excluded, as it is lower than the C/2- and C-rates) due to the electrode polarization that decreased the Li^+ ion diffusion and the electronic conductivity in the structure. The C/5 behavior is explained by the ohmic polarization through the SEI formed at the initial cycles, as it may be inferred from Figure 7d. The discharge capacities calculated for each C-rate and for the cocoon separators upon exposure to plasma for 30 s are: 96.7, 110.7, 118.5, 120.2 and 112.0 mAh g^{-1} at 5C, 2C, C, C/2 and C/5 rates, respectively.

The 5C-rate profile discharge curves for all the samples are represented in Figure 8b. As mentioned above, all the samples display the same profile. On the other hand, the discharge capacity values change among them. Independently of the exposure time, the plasma treatment led to a marked increase of the discharge capacity. The discharge capacity values for the cocoon separators were 26.1, 56.6, 96.7, 76.9 and 57.4 mAh g^{-1} for plasma exposures of 0, 15, 30, 50 and 100 s, respectively. For the plasma treatment time at the 5C-rate, the higher the ionic conductivity (Figure 7c), the higher the discharge capacity value, demonstrating that the ionic conductivity component is intimately correlated, as expected, with the battery electrochemical performance.

The discharge rate performance of the cocoon separators at the studied rates was also evaluated. Figure 8c reveals that at low C-rates the discharge capacity values remained practically the same (between around 105 and 125 $mAhg^{-1}$). It also shows that the increase of the C-rates led to more evident differences between the separators exposed to different plasma times. The cocoon separator plasma-treated for 30 s exhibited the highest discharge capacity value at the fastest rate.

The capacity retention of the samples discharge process as a function of the different C-rates considered is represented in Figure 8d. The capacity retention was normalized to the C/5-rate and the results show that upon increasing the C-rates, the capacity retention decreases due to the different Li^+ diffusion [69]. Despite this, the cocoon treated for 30 s showed just a 13% decrease of its own capacity, pointing out the good separator applicability in LIBs. The high ionic conductivity and reduced overall resistance of the cocoon separator in the battery are the mains reasons behind this behavior. Furthermore, the overall resistance of the half-cells before cycling (Figure 7d) reveals that the cocoon separator plasma-treated for 30 s presented in addition lower battery resistance.

To assess the cycling performance of the prepared half-cell batteries including the plasma-treated cocoons separators, 55 cycles at 2C- and 5C-rates were performed.

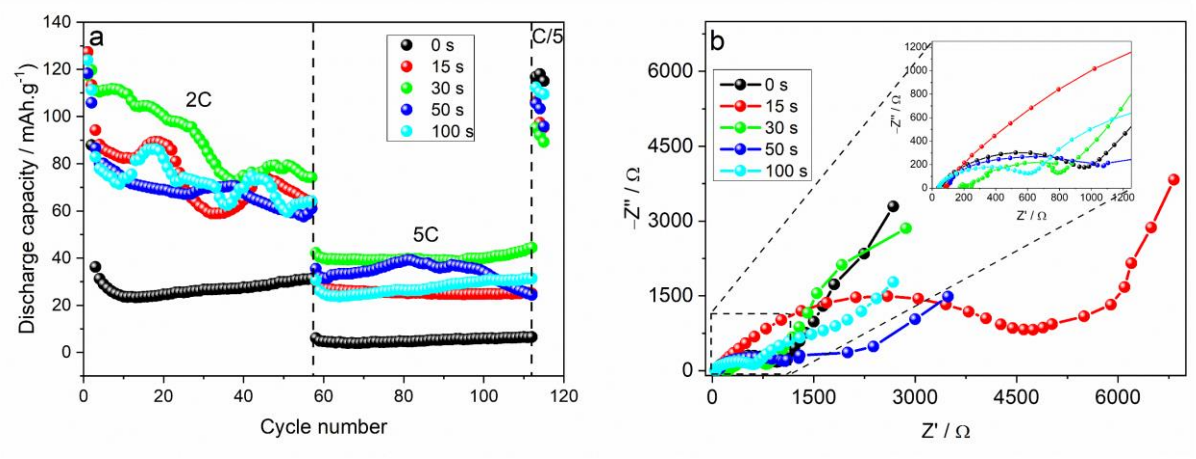

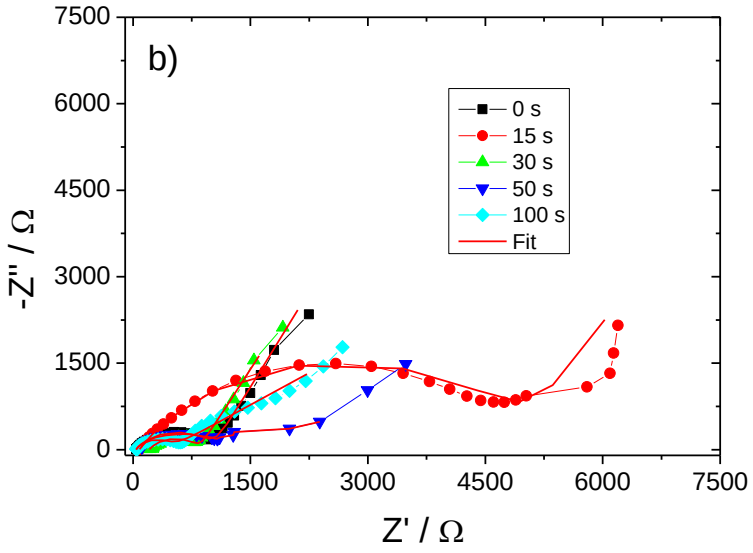

Figure 9. (a) Discharge capacity at 2C- and 5C-rates, and (b) EIS after cycling of the half-cell batteries assembled with the cocoons separators exposed to different plasma treatment times and corresponding fit with the equivalent circuit presented in the inset of Figure 7d..

Figure 9a shows that the discharge capacity after 55 cycles were 31.3, 63.5, 74.2, 61.0 and 64.2 mAh g^{-1} at 2C-rate, and 6.5, 25.0, 44.4, 24.4 and 31.4 mAh g^{-1} at 5C-rate for plasma treatment times of 0, 15, 30, 50 and 100 s, respectively. The observed cycling stability at 2C-rate is related to the charge transfer kinetics, whereas at 5C-rate the Li^+ diffusion is the dominant effect [69].

According to these findings, the change of capacity during the cycles is due to the different room temperatures over the time, once the charge transfer kinetics is related to the temperature. On the other hand, at 5C-rate the separators with higher ionic conductivity and less overall resistance denote higher discharge capacity value.

From the data obtained from the cycling impedance measurements of the half-cell batteries reproduced in Figure 9b we may infer that the overall resistances of the separators were 957, 4605, 790, 1076 and 627 Ω for plasma treatments of 0, 15, 30, 50 and 100 s, respectively. Comparison of the results of the half-cells impedance before (Figure 7d) and after (Figure 9b) cycling, allows concluding that, except for the half-cell with the cocoon plasma treated for 100 s, the overall resistance of the batteries increased after the cycling process, indicating the formation of a stable SEI (better Li^+ diffusion). Although the half-cell prepared with the cocoon separator plasma-treated for 100 s evidences a low overall resistance after cycling, the separator itself presents the lowest uptake value (Figure 7a) and the lowest ionic conductivity (Figure 7c) of all the plasma-treated samples, yielding a poorer battery performance compared, for example, with that prepared with the sample plasma-treated for 30 s. The high overall resistance of the half-cell with the cocoon treated with plasma for 15 s (Figure 9b) is indicative of the low Li^+ diffusion capacity between the interface of the cathode and the separator, despite its good ionic conductivity (Figure 7c).

Commercial separators based on polyolefins (Polyethylene, PE, and polypropylene, PP) present some disadvantages, such as low wettability, thermal instability and being highly flammable. To improve those issues, different surface treatments such as plasma treatment and coating have been explores for those separators. Table 1 shows the electrochemical parameters of the cocoon's separators developed in the present work, together with the ones from representative commercial separators for cathodic half-cells with LFP as active material.

Table 1: Electrochemical parameters of surface treated Bombyx mori silkworm cocoon (this work) and polyolefins separator membranes in LFP cathodic half-cells.

Separator	**Modification treatment**	**Electrolyte solution**	**Conductivity (mS cm^{-1})**	**Discharge capacity (mAh g^{-1})**	**Ref**
PP	PVdF-HFP-Pluronic F127 + SiO_2	1 M $LiPF_6$ in EC:DEC:DMC	1.76	130	Xiaofei Li, Jinlin He, Dazhao Wu,

	nanoparticles and 10 s plasma treatment	(1:1:1, vol.)			Mingzu Zhang, Juwen Meng, Peihong Ni, Development of plasma-treated polypropylene nonwoven-based composites for high-performance lithium-ion battery separators, Electrochimica Acta, Volume 167, 2015, Pages 396-403,
PP	Coating with ZrO_2 and PDA/PEI	1 M $LiPF_6$ in EC:DEC:DMC (1:1:1, vol.)	1.61	Coating of ZrO_2 ≈ 125 (2C) ≈ 100 (5C) Coating of PDA/PEI ≈ 100 (2C)	J.-K. Pi, G.-P. Wu, H.-C. Yang, C.G. Arges, Z.-K. Xu, Separators with biomineralized

				≈ 60 (5C)	zirconia coatings for enhanced thermo- and electro-performance of lithium-ion batteries, ACS Appl. Mater. Interfaces 9 (2017) 21971–21978
PE	Coating with TiO_2-PMMA	1 M $LiPF_6$ in EC:DMC (1:1, vol.)	0.87	110 (2C)	Y. Xi, P. Zhang, H. Zhang, Z. Wan, W. Tu, H. Tang, Membrane separators coated by TiO2-PMMA with low thermal shrinkage rate for lithium-ion batteries, Int. J. Electrochem. Sci. 12

					(2017) 5421–5430.
PE	Coating with SiO_2 and SBA-15-PVDF	1 M $LiPF_6$ in EC:DMC (1:1, vol.)	-	121 (2C)	S. Prabhavathy, P.K. Sen, S. Sivaprakash, Enhanced electrochemical performance of nanoparticle coated polyethylene separator surface for lithium-ion batteries, Mater. Res. Express 1 (2014), 045504.
PE	Grafting of TiO_2	1 M $LiPF_6$ in EC:DMC:DEC, (1:1:1, vol)	0.5	≈ 110 (2C) ≈ 80 (5C)	X. Zhu, X. Jiang, X. Ai, H. Yang, Y. Cao, TiO2 ceramic-grafted polyethylene separators for enhanced thermostabilit

					y and electrochemical performance of lithium-ion batteries, J. Membr. Sci. 504 (2016) 97–103.
PE	60 s of O_2 plasma treatment	1 M $LiPF_6$ in EC: DMC (1:1, vol.)	-	≈ 90 (2C)	Jin, S. Y., Manuel, J., Zhao, X., Park, W. H., & Ahn, J.-H. (2017). Surface-modified polyethylene separator via oxygen plasma treatment for lithium ion battery. Journal of Industrial and Engineering Chemistry, 45, 15–21.

Bombyx mori silkworm cocoon	30 s of O_2 plasma treatment	1 M $LiPF_6$ in EC: DMC (1:1, vol.)	2.33	110.7 (2C) 96.7 (5C)	This Work

The different approaches used to improve the separator parameters (Table 1) are in some cases a combination of processes and/or materials, which can be a disadvantage. Together with the main advantages of plasma treatments in battery separator membranes mentioned in section 3.1, they also enhance the electrochemical performance of the separator, showing the relevance of this fast, affordable and safe surface treatment.

4. Conclusions

In the present work we report a fast and eco-friendly surface modification of *Bombyx mori* cocoons-based separators by two plasmas (O_2 and N_2) applied at different exposure times. Upon plasma exposure the behavior of the separators changed dramatically from superhydrophobic to superhydrophilic (the water contact angle became virtually 0°). This effect had obvious beneficial consequences in terms of wettability and wicking, without jeopardizing, however, the flammability behavior and thus safety issues. While the SEM images did not reveal any visible modification of the silk fibers at the macroscale, the AFM measurements provided unequivocal evidences of marked topographical changes at the submicroscale. In particular, a unique etching process was identified, which involved the cocoon nanofibrils, an indication that at least the 5^{th} hierarchical level of silk was deeply affected by the plasma treatment. Due to the higher O_2 reactivity with respect to N_2, the O_2 plasma treatment resulted in a more effective and faster etching than that caused by the N_2 plasma-treated samples. For this reason, the remaining of the study was focused exclusively on the samples treated with O_2 plasma. Apart from the physical impact, exposure to O_2 plasma also led to chemical modifications, although subtle, at the surface of the cocoon separators. In the case of the cocoon treated for 30 s these modifications were manifested in the increase of the oxygen element (30 ± 2 %), due to the emergence of oxygen-containing functionalities. Accordingly, several features of the raw cocoon separator were affected by exposure to O_2 plasma. The electrolyte uptake maximum value decreased from 400 to around 250-350%, but the necessary time to reach this maximum uptake value was reduced from 2 min to just 15 s, respectively. Not surprisingly, the ionic

conductivity of the raw cocoon was enhanced upon O_2 plasma treatment. The latter finding may be correlated with the fact that the negatively charged surface of plasma-treated separators is known to increase the mobility of Li^+ ions and contribute to the uniformity of the SEI layer [38, 70]. At 25 ºC the cocoon separator exposed for 30 s exhibited the highest ionic conductivity (2.33 mS cm^{-1}) of all the O_2 plasma-treated samples.

The half-cells assembled with the plasma-treated cocoon separators showed different electrochemical performance. The lower overall resistance and the good cycling performance suggest good Li^+ mobility and stable SEI formation. For high C-rates (5C) the influence of the O_2 plasma treatment was definitely more evident, the cocoon separator treated for 30 s yielding the highest discharge capacity (96.7 mAh g^{-1}) and the highest capacity retention (87.2%). These findings clearly point out the tremendous technological potential of this optimized cocoon separator sample in LIBs, as long as the discharge capacity is kept over the C-rates.

Furthermore, we must emphasize that the half-cell battery incorporating the cocoon separator exposed to O_2 plasma for 30 s denoted an unprecedented performance improvement with respect to the battery including the raw cocoon separator, the figures of merit being an outstanding increase of the discharge capacity of ca. 270% (from 26.1 to 96.7 mAh g^{-1} at 5C-rate) and an even more impressive increase of the capacity retention (normalized with respect to the C/5 rate) of ca. 291% (from 22.3 to 87.2%). These truly extraordinary figures are intimately associated with the high electrolyte uptake value (289%), the high ionic conductivity, and the low overall resistance before and after cycling offered by this optimized cocoon separator.

At last, it is of interest to compare the present figures of merit with those reported for systems including commercial separators. At 2C-rate the discharge capacity value of the half-cell including the optimized cocoon separator is slightly higher (110.7 versus 105.0 mAh g^{-1} [71]), whereas at 5C-rate it undergoes a 3.5-fold increase (96.7 versus 27.4 mAh g^{-1} [72]).

Acknowledgments

This work was supported by National funds by Foundation for Science and Technology (FCT) in the framework of the Strategic Funding UID/FIS/04650/2019, UID/QUI/00686/2016, UID/QUI/00686/2018 and UID/QUI/00686/2019. The authors thank FEDER funds through the COMPETE 2020 Program and National Funds through FCT under the projects PTDC/FIS-

MAC/28157/2017, PEst-OE/QUI/UI0616/2014, LUMECD (POCI-01-0145-FEDER-016884 and PTDC/CTM-NAN/0956/2014), UniRCell (SAICTPAC/0032/2015 and POCI-01-0145-FEDER-016422), Investigator FCT Contract CEECIND/00833/2017 (R.G.) and grants SFRH/BPD/87759/2012 (R.F.P.P), SFRH/BPD/121526/2016 (D.M.C) and SFRH/BPD/112547/2015 (C.M.C). R.F.P.P. also thanks FCT-UM for the researcher contract in the scope of Decreto-Lei 57/2016 and 57/2017. H.M.R. acknowledges financial support from PTDC/BTM-MAT/30858/2017. Funding by Basque Government Industry and Education Department under the ELKARTEK, HAZITEK and PIBA programs is acknowledged.

References

[1] The Nobel Prize in Chemistry 2019. https://www.nobelprize.org/prizes/chemistry/2019/summary (accessed 18-10-2019).

[2] T. Kim, W. Song, D.-Y. Son, L.K. Ono, Y. Qi, Lithium-ion batteries: outlook on present, future, and hybridized technologies, J. Mater. Chem. A, 7 (2019) 2942-2964.

[3] M. Li, J. Lu, Z. Chen, K. Amine, 30 Years of Lithium-Ion Batteries, Adv. Mater., 30 (2018) 1800561.

[4] N. Nitta, F. Wu, J.T. Lee, G. Yushin, Li-ion battery materials: present and future, Mater. Today, 18 (2015) 252-264.

[5] B. Dunn, H. Kamath, J.-M. Tarascon, Electrical energy storage for the grid: a battery of choices, Science, 334 (2011) 928-935.

[6] J.B. Goodenough, Y. Kim, Challenges for rechargeable Li batteries, Chem. Mat., 22 (2010) 587-603.

[7] M. Armand, J.M. Tarascon, Building better batteries, Nature, 451 (2008) 652-657.

[8] H. Zhang, M.-Y. Zhou, C.-E. Lin, B.-K. Zhu, Progress in polymeric separators for lithium ion batteries, RSC Adv., 5 (2015) 89848-89860.

[9] M.F. Lagadec, R. Zahn, V. Wood, Characterization and performance evaluation of lithium-ion battery separators, Nat. Energy, 4 (2019) 16-25.

[10] H. Zhang, H. Zhao, M.A. Khan, W. Zou, J. Xu, L. Zhang, J. Zhang, Recent progress in advanced electrode materials, separators and electrolytes for lithium batteries, J. Mater. Chem. A, 6 (2018) 20564-20620.

[11] C.M. Costa, Y.-H. Lee, J.-H. Kim, S.-Y. Lee, S. Lanceros-Méndez, Recent advances on separator membranes for lithium-ion battery applications: From porous membranes to solid electrolytes, Energy Storage Mater., 22 (2019) 346-375.

[12] A.T. Nguyen, Q.-L. Huang, Z. Yang, N. Lin, G. Xu, X.Y. Liu, Crystal networks in silk fibrous materials: from hierarchical structure to ultra performance, Small, 11 (2015) 1039-1054.

[13] A. Girotti, D. Orbanic, A. Ibáñez-Fonseca, C. Gonzalez-Obeso, J.C. Rodríguez-Cabello, Recombinant technology in the development of materials and systems for soft-tissue repair, Adv. Healthc. Mater., 4 (2015) 2423-2455.
[14] L. Meinel, D.L. Kaplan, Silk constructs for delivery of musculoskeletal therapeutics, Adv. Drug Delivery Rev., 64 (2012) 1111-1122.
[15] R.F.P. Pereira, M.M. Silva, V. de Zea Bermudez, *Bombyx mori* silk fibers: an outstanding family of materials, Macromol. Mater. Eng., 300 (2015) 1171-1198.
[16] S. Hazra, S. Nandi, D. Naskar, R. Guha, S. Chowdhury, N. Pradhan, S.C. Kundu, A. Konar, Non-mulberry Silk Fibroin Biomaterial for Corneal Regeneration, Sci. Rep., 6 (2016) 21840.
[17] A. Kiseleva, G. Kiselev, V. Kessler, G. Seisenbaeva, D. Gets, V. Rumyantseva, T. Lyalina, A. Fakhardo, P. Krivoshapkin, E. Krivoshapkina, Optically active hybrid materials based on natural spider silk, ACS Appl. Mater. Interfaces, 11 (2019) 22962-22972.
[18] M. Zourob, J.E. Gough, R.V. Ulijn, A micropatterned hydrogel platform for chemical synthesis and biological analysis, Adv. Mater., 18 (2006) 655-659.
[19] M. Wang, H.-G. Braun, T. Kratzmüller, E. Meyer, Patterning polymers by micro-fluid-contact printing, Adv. Mater., 13 (2001) 1312-1317.
[20] B.D. Lawrence, M. Cronin-Golomb, I. Georgakoudi, D.L. Kaplan, F.G. Omenetto, Bioactive silk protein biomaterial systems for optical devices, Biomacromolecules, 9 (2008) 1214-1220.
[21] S.T. Parker, P. Domachuk, J. Amsden, J. Bressner, J.A. Lewis, D.L. Kaplan, F.G. Omenetto, Biocompatible silk printed optical waveguides, Adv. Mater., 21 (2009) 2411-2415.
[22] J.J. Amsden, P. Domachuk, A. Gopinath, R.D. White, L.D. Negro, D.L. Kaplan, F.G. Omenetto, Rapid nanoimprinting of silk fibroin films for biophotonic applications, Adv. Mater., 22 (2010) 1746-1749.
[23] N. Qi, B. Zhao, S.-D. Wang, S.S. Al-Deyab, K.-Q. Zhang, Highly flexible and conductive composite films of silk fibroin and silver nanowires for optoelectronic devices, RSC Adv., 5 (2015) 50878-50882.
[24] C. Müller, M. Hamedi, R. Karlsson, R. Jansson, R. Marcilla, M. Hedhammar, O. Inganäs, Woven electrochemical transistors on silk fibers, Adv. Mater., 23 (2011) 898-901.
[25] S. Ling, C. Li, K. Jin, D.L. Kaplan, M.J. Buehler, Liquid exfoliated natural silk nanofibrils: Applications in optical and electrical devices, Adv. Mater., 28 (2016) 7783-7790.
[26] R.F.P. Pereira, F. Sentanin, A. Pawlicka, M.C. Gonçalves, M.M. Silva, V. de Zea Bermudez, Smart windows prepared from *Bombyx mori* silk, ChemElectroChem, 3 (2016) 1084-1097.
[27] I.S. Romero, N.P. Bradshaw, J.D. Larson, S.Y. Severt, S.J. Roberts, M.L. Schiller, J.M. Leger, A.R. Murphy, Biocompatible electromechanical actuators composed of silk-conducting polymer composites, Adv. Funct. Mater., 24 (2014) 3866-3873.
[28] J. Hou, C. Cao, F. Idrees, X. Ma, Hierarchical porous nitrogen-doped carbon nanosheets derived from silk for ultrahigh-capacity battery anodes and supercapacitors, ACS Nano, 9 (2015) 2556-2564.

[29] X. Jia, C. Wang, C. Zhao, Y. Ge, G.G. Wallace, Toward biodegradable Mg–air bioelectric batteries composed of silk fibroin–polypyrrole film, Adv. Funct. Mater., 26 (2016) 1454-1462.
[30] X. Jia, C. Wang, V. Ranganathan, B. Napier, C. Yu, Y. Chao, M. Forsyth, F.G. Omenetto, D.R. MacFarlane, G.G. Wallace, A biodegradable thin-film magnesium primary battery using silk fibroin–ionic liquid polymer electrolyte, ACS Energy Lett., 2 (2017) 831-836.
[31] R.F.P. Pereira, R. Brito-Pereira, R. Gonçalves, M.P. Silva, C.M. Costa, M.M. Silva, V. de Zea Bermudez, S. Lanceros-Méndez, Silk fibroin separators: A step toward lithium-ion batteries with enhanced sustainability, ACS Appl. Mater. Interfaces, 10 (2018) 5385-5394.
[32] R.F.P. Pereira, R. Gonçalves, M. Fernandes, C.M. Costa, M.M. Silva, V. de Zea Bermudez, S. Lanceros-Mendez, *Bombyx mori* silkworm cocoon separators for lithium-ion batteries with superior safety and sustainability, Adv. Sustainable Syst., 2 (2018) 1800098.
[33] D.N. Rockwood, R.C. Preda, T. Yucel, X. Wang, M.L. Lovett, D.L. Kaplan, Materials fabrication from *Bombyx mori* silk fibroin, Nat. Protocols, 6 (2011) 1612-1631.
[34] J. Zhang, R. Rajkhowa, J.L. Li, X.Y. Liu, X.G. Wang, Silkworm cocoon as natural material and structure for thermal insulation, Mater. Des., 49 (2013) 842-849.
[35] B. Tulachan, S.K. Meena, R.K. Rai, C. Mallick, T.S. Kusurkar, A.K. Teotia, N.K. Sethy, K. Bhargava, S. Bhattacharya, A. Kumar, R.K. Sharma, N. Sinha, S.K. Singh, M. Das, Electricity from the silk cocoon membrane, Sci. Rep., 4 (2014) 5434.
[36] B. Tulachan, S. Srivastava, T.S. Kusurkar, N.K. Sethy, K. Bhargava, S.K. Singh, D. Philip, A. Bajpai, M. Das, The role of photo-electric properties of silk cocoon membrane in pupal metamorphosis: A natural solar cell, Sci. Rep., 6 (2016) 21915.
[37] S.Y. Jin, J. Manuel, X. Zhao, W.H. Park, J.-H. Ahn, Surface-modified polyethylene separator via oxygen plasma treatment for lithium ion battery, J. Ind. Eng. Chem., 45 (2017) 15-21.
[38] M. Han, D.-W. Kim, Y.-C. Kim, Charged polymer-coated separators by atmospheric plasma-induced grafting for lithium-ion batteries, ACS Appl. Mater. Interfaces, 8 (2016) 26073-26081.
[39] W. Sangprasert, V.S. Lee, D. Boonyawan, K. Tashiro, P. Nimmanpipug, Sulfur hexafluoride plasma surface modification of Gly-Ala and Ala-Gly as *Bombyx mori* silk model compounds: mechanism investigations, J. Mol. Struct., 963 (2010) 130-136.
[40] D. Gogoi, J. Chutia, A.J. Choudhury, A.R. Pal, D. Patil, Radio-frequency Ar plasma treatment on muga silk fiber: correlation between physicochemical and surface morphology, J. Theor. Appl. Phys., 6 (2012) 39.
[41] K.M.M. Rahman, L. Zou, M. Miura, H. Morikawa, M. Zha, M. Iwasa, Surface morphology of low-temperature argon-plasma-treated *Bombyx mori* silk fibroin fiber, J. Silk Sci. Tech. Jpn., 16 (2007) 107-114.
[42] K.V. Rani, N. Chandwani, P. Kikani, S.K. Nema, A.K. Sarma, B. Sarma, Optimization and surface modification of silk fabric using DBD air plasma for improving wicking properties, J. Text. I., 109 (2018) 368-375.

[43] Y. Iriyama, T. Mochizuki, M. Watanabe, M. Utada, Plasma treatment of silk fabrics for better dyeability, J. Photopolym. Sci. Technol., 15 (2002) 299-306.
[44] L. Jeong, I.-S. Yeo, H.N. Kim, Y.I. Yoon, D.H. Jang, S.Y. Jung, B.-M. Min, W.H. Park, Plasma-treated silk fibroin nanofibers for skin regeneration, Int. J. Biol. Macromol., 44 (2009) 222-228.
[45] C.-w. Kan, Y.-l. Lam, The effect of plasma treatment on water absorption properties of silk fabrics, Fibers Polym., 16 (2015) 1705-1714.
[46] A. Gören, J. Mendes, H.M. Rodrigues, R.E. Sousa, J. Oliveira, L. Hilliou, C.M. Costa, M.M. Silva, S. Lanceros-Méndez, High performance screen-printed electrodes prepared by a green solvent approach for lithium-ion batteries, J. Power Sources, 334 (2016) 65-77.
[47] M. Parvinzadeh Gashti, Surface modification of synthetic fibers to improve performance: Recent approaches, Global J. Phys. Chem., 3 (2012) 1-10.
[48] L. Duque Sánchez, N. Brack, A. Postma, P.J. Pigram, L. Meagher, Surface modification of electrospun fibres for biomedical applications: A focus on radical polymerization methods, Biomaterials, 106 (2016) 24-45.
[49] D. Sun, Surface modification of natural fibers using plasma treatment, in: S. Kalia (Ed.) Biodegradable Green Composites, John Wiley & Sons, Inc.2016, pp. 18-39.
[50] N. Inagaki, Plasma Surface Modification and Plasma Polymerization, 1st Edition ed., Technomic Publishing Company, Inc., Basel, Switzerland, 1996.
[51] H. Yasuda, Plasma polymerization, Academic Press, New York, 1985.
[52] K. Masayuki, S. Yasushi, K. Shin-ichi, Y. Yukinori, Novel application of plasma treatment for pharmaceutical and biomedical engineering, Curr. Drug Discov. Technol., 6 (2009) 135-150.
[53] G. Nageswaran, A. Sureshkumar, S. Neogi, RF plasma-treated polymers for biomedical applications, Curr. Sci., 94 (2008).
[54] W. Qiu, A. Patil, F. Hu, X.Y. Liu, Hierarchical structure of silk materials versus mechanical performance and mesoscopic engineering principles, Small, (2019) 1903948.
[55] S. Ling, D.L. Kaplan, M.J. Buehler, Nanofibrils in nature and materials engineering, Nat. Rev. Mater., 3 (2018) 18016.
[56] N. Lin, X.Y. Liu, Correlation between hierarchical structure of crystal networks and macroscopic performance of mesoscopic soft materials and engineering principles, Chem. Soc. Rev., 44 (2015) 7881-7915.
[57] Q. Wang, H.C. Schniepp, Nanofibrils as building blocks of silk fibers: critical review of the experimental evidence, JOM, 71 (2019) 1248-1263.
[58] H.-P. Zhao, X.-Q. Feng, H. Gao, Ultrasonic technique for extracting nanofibers from nature materials, Appl. Phys. Lett., 90 (2007) 073112.
[59] X. Tan, W. Zhao, T. Mu, Controllable exfoliation of natural silk fibers into nanofibrils by protein denaturant deep eutectic solvent: nanofibrous strategy for multifunctional membranes, Green Chem., 20 (2018) 3625-3633.

[60] G. Xu, L. Gong, Z. Yang, X.Y. Liu, What makes spider silk fibers so strong? From molecular-crystallite network to hierarchical network structures, Soft Matter, 10 (2014) 2116-2123.
[61] J. Pérez-Rigueiro, M. Elices, G.R. Plaza, G.V. Guinea, Similarities and differences in the dupramolecular organization of silkworm and spider silk, Macromolecules, 40 (2007) 5360-5365.
[62] G.R. Plaza, P. Corsini, E. Marsano, J. Pérez-Rigueiro, L. Biancotto, M. Elices, C. Riekel, F. Agulló-Rueda, E. Gallardo, J.M. Calleja, G.V. Guinea, Old silks endowed with new properties, Macromolecules, 42 (2009) 8977-8982.
[63] T.-Y. Lin, H. Masunaga, R. Sato, A.D. Malay, K. Toyooka, T. Hikima, K. Numata, Liquid crystalline granules align in a hierarchical structure to produce dpider dragline microfibrils, Biomacromolecules, 18 (2017) 1350-1355.
[64] P. Amornsudthiwat, S. Damrongsakkul, Oxygen plasma etching of silk fibroin alters surface stiffness: A cell–substrate interaction study, Plasma Process Polym., 11 (2014) 763-776.
[65] L. Zhou, X. Chen, W. Dai, Z. Shao, X-ray photoelectron spectroscopic and Raman analysis of silk fibroin–Cu(II) films, Biopolymers, 82 (2006) 144-151.
[66] C. Riccardi, R. Barni, P. Esena, Plasma treatment of silk, Solid State Phenom., 107 (2005) 125-128.
[67] L. Zhu, W. Xu, M. Ma, H. Zhou, Effect of plasma treatment of silk fibroin powder on the properties of silk fibroin powder/polyurethane blend film, Polym. Eng. Sci., 50 (2010) 1705-1712.
[68] C. Fongy, A.-C. Gaillot, S. Jouanneau, D. Guyomard, B. Lestriez, Ionic vs electronic power limitations and analysis of the fraction of wired grains in $LiFePO_4$ composite electrodes, J. Electrochem. Soc., 157 (2010) A885-A891.
[69] J.B. Habedank, L. Kraft, A. Rheinfeld, C. Krezdorn, A. Jossen, M.F. Zaeh, Increasing the discharge rate capability of lithium-ion cells with laser-structured graphite anodes: Modeling and simulation. J. Electrochem. Soc., 165 (2018) A1563-A1573.
[70] J.H. Ahn, H.-J. Shin, S. Abbas, K.-Y. Lee, H.Y. Ha, Plasma-functionalized carbon-layered separators for improved performance of lithium sulfur batteries, J. Mater. Chem. A, 7 (2019) 3772-3782.
[71] C.M. Costa, H.M. Rodrigues, A. Gören, A.V. Machado, M.M. Silva, S. Lanceros-Méndez, Preparation of poly(vinylidene fluoride) lithium-ion battery separators and their compatibilization with ionic liquid – A green solvent approach, ChemistrySelect, 2 (2017) 5394-5402.
[72] R.E. Sousa, J. Oliveira, A. Gören, D. Miranda, M.M. Silva, L. Hilliou, C.M. Costa, S. Lanceros-Mendez, High performance screen printable lithium-ion battery cathode ink based on C-$LiFePO_4$, Electrochim. Acta, 196 (2016) 92-100.

Appendix A

Table A.1. Elemental composition (C, O and N) and ratios (O/C, O/N and C/N) on the surface of *Bombyx mori* cocoons (0 s) and after different O_2 and N_2 plasma treatment times (15, 30, 50 and 100 s).

		Elemental composition (%)			Elemental ratios		
		C	***O***	***N***	***O/C***	***O/N***	***N/C***
	0 s	67.3 ± 0.9	19.9 ± 0.9	12.8 ± 0.6	0.29 ± 0.01	1.55 ± 0.09	0.191 ± 0.009
O_2	**15 s**	60.1 ± 0.5	26.7± 0.2	13.2 ± 0.5	0.444 ± 0.005	2.02 ± 0.08	0.220 ± 0.008
	30 s	57 ± 3	30 ± 2	14 ± 1	0.52 ± 0.05	2.2 ± 0.3	0.24 ± 0.03
	50 s	58 ± 1	27 ± 1	15.2 ± 0.5	0.47 ± 0.02	1.78 ± 0.08	0.26 ± 0.01
	100 s	54 ± 1	28.3 ± 0.8	15.3 ± 0.9	0.50 ± 0.02	1.8 ± 0.1	0.27 ± 0.02
N_2	**15 s**	57 ± 1	31.8 ± 0.8	10.4 ± 0.7	0.55 ± 0.02	3.1± 0.2	0.180 ± 0.01
	30 s	51 ± 2	34.1 ± 0.9	15.1 ± 0.8	0.67 ± 0.02	2.3 ± 0.1	0.30 ± 0.02
	50 s	56 ± 4	31.6 ± 2	12.6 ± 2	0.56 ± 0.05	2.5 ± 0.4	0.23 ± 0.04
	100 s	47.9 ± 0.8	35.8 ± 0.8	16.4 ± 0.3	0.75 ± 0.02	2.2 ± 0.06	0.343 ± 0.008

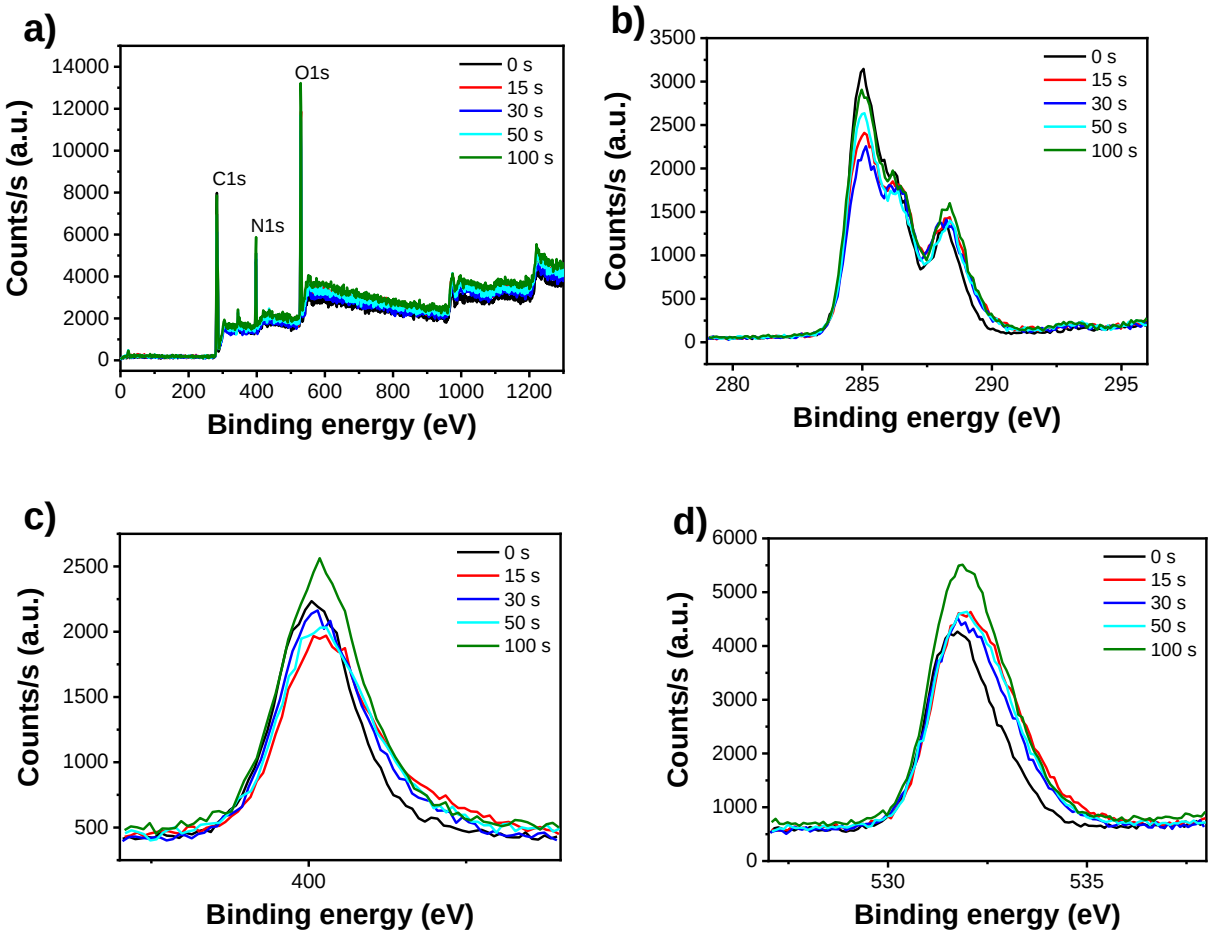

Figure A.1. Examples of XPS spectrum of raw *Bombyx mori* cocoons and treated under oxygen at different treatment times: (a) wide spectra and the corresponding expansion of (b) C1s (b) N1a and (d) O1s peaks.

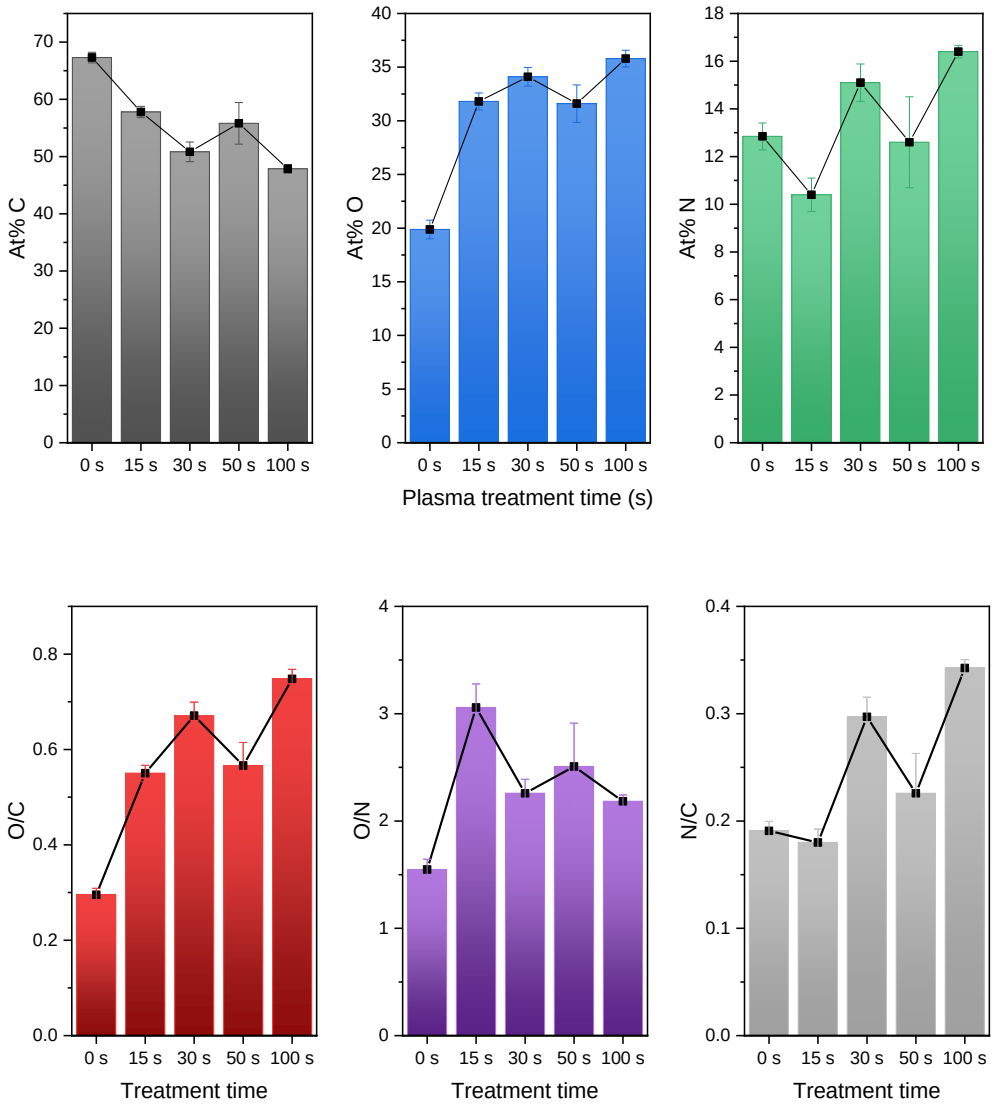

Figure A.2. Elemental composition (C – grey bars, O – blue bars, N – green bars) (A) and elemental ratios (C/O – red bars, O/N – violet bars, and C/N – light grey bars) at the surface of *Bombyx mori* cocoons as a function of N_2 plasma exposure time.

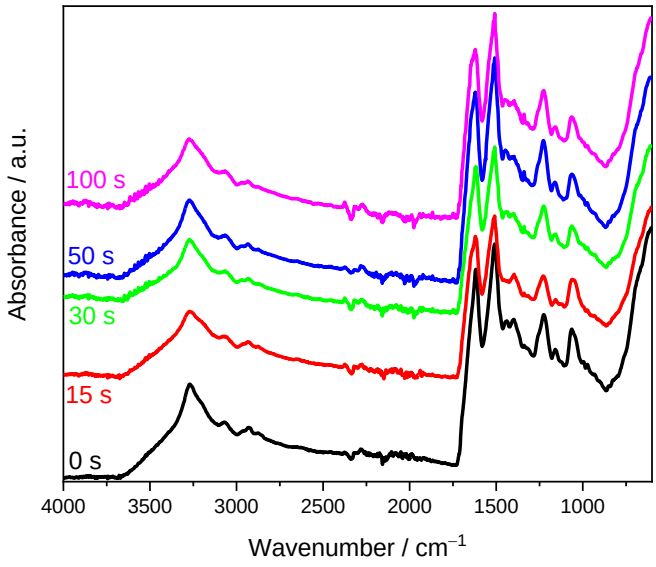

Figure A.3. ATR/FT-IR spectra of the *Bombyx mori* cocoons in the range 4000-600 cm^{-1}: raw (black line) and treated with O_2 plasma with different exposure times.

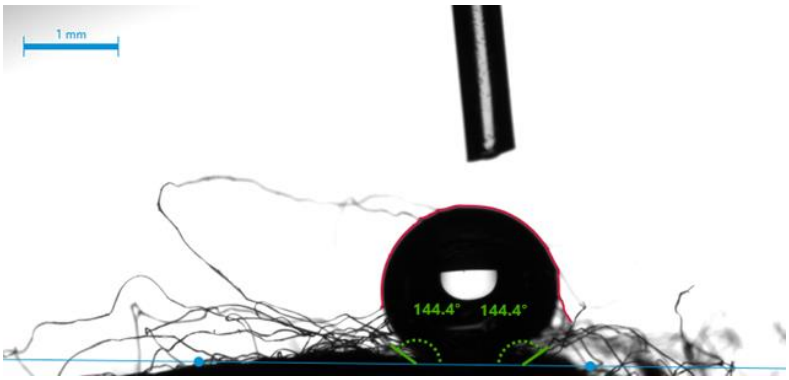

Figure A.4. Image of the contact angle in the outer surface of an untreated *Bombyx mori* separator.